Glutamatergic and GABAergic neurons mediate distinct neurodevelopmental phenotypes of *STXBP1* encephalopathy

Joo Hyun Kim[1,2], Wu Chen[1,2], Eugene S. Chao[1,2], Hongmei Chen[1,2], Mingshan Xue[1,2,3*]

[1]Department of Neuroscience, Baylor College of Medicine, Houston, Texas 77030, USA

[2]The Cain Foundation Laboratories, Jan and Dan Duncan Neurological Research Institute at Texas Children's Hospital, Houston, Texas 77030, USA

[3]Department of Molecular and Human Genetics, Baylor College of Medicine, Houston, Texas 77030, USA

*Correspondence: mxue@bcm.edu

Abstract (149 words)

Heterozygous pathogenic variants in syntaxin-binding protein 1 (STXBP1, also known as MUNC18-1) cause *STXBP1* encephalopathy and are among the most frequent causes of developmental and epileptic encephalopathies and intellectual disabilities. STXBP1 is an essential protein for presynaptic neurotransmitter release, and its haploinsufficiency impairs glutamatergic and GABAergic neurotransmission. However, the mechanism underlying the broad spectrum of neurological phenotypes is poorly understood. Here we show that glutamatergic and GABAergic neurons mediate distinct disease features with few overlaps. Glutamatergic and GABAergic neurons-specific *Stxbp1* haploinsufficient mice exhibit different subsets of the cognitive and seizure phenotypes observed in the constitutive *Stxbp1* haploinsufficient mice. Developmental delay and most of the motor and psychiatric phenotypes are only recapitulated by GABAergic *Stxbp1* haploinsufficiency. Thus, the contrasting roles of

24 excitatory and inhibitory signaling in *STXBP1* encephalopathy identify GABAergic dysfunction
25 as a main disease mechanism and reveal the possibility to selectively modulate disease
26 phenotypes by targeting specific neurotransmitter systems.
27
28 **Introduction**
29 Synaptic dysfunction is a hallmark of many neurological disorders (Brose et al., 2010; Lepeta et
30 al., 2016). Pathogenic variants in synaptic proteins may collectively account for more
31 neurological disorders than any other functional group of proteins (Grant, 2019). More recently,
32 an increasing number of mutations in presynaptic proteins are being discovered in
33 neurodevelopmental disorders. These proteins are involved in different steps of the synaptic
34 vesicle cycle–tethering, docking, priming, fusion, and recycling (Verhage and Sørensen, 2020;
35 Bonnycastle et al., 2021; John et al., 2021; Melland et al., 2021). The clinical features of these
36 synaptic vesicle cycle disorders are diverse, but the most prevalent features include intellectual
37 disability, epilepsy, movement disorders, cerebral visual impairment, and psychiatric symptoms
38 (Verhage and Sørensen, 2020; John et al., 2021). Although the molecular and cellular functions
39 of many of these presynaptic proteins are well understood, the disease pathogeneses remain
40 elusive. Thus, in-depth neurological studies in disease models with genetic and phenotypic
41 accuracy are necessary to elucidate the neural mechanisms underlying neurodevelopmental
42 deficits and develop therapeutic strategies.
43
44 Among this growing list of synaptic vesicle cycle disorders, *STXBP1* encephalopathy is the most
45 frequent and caused by *de novo* heterozygous *STXBP1* mutations (Verhage and Sørensen, 2020;
46 John et al., 2021). In fact, pathogenic variants in *STXBP1* are among the top 5 causes of pediatric

47 epilepsy (Symonds and McTague, 2020) and top 10 causes of neurodevelopmental disorders
48 (Deciphering Developmental Disorders Study, 2015; Kaplanis et al., 2020). All *STXBP1*
49 encephalopathy patients have intellectual disability, and more than 80–90% of patients have
50 epilepsy and motor dysfunctions (Stamberger et al., 2016; Abramov et al., 2020). Other less
51 common clinical features include developmental delay, autistic traits, hyperactivity, anxiety, and
52 aggressive behaviors (Stamberger et al., 2016; Suri et al., 2017). Since about 60% of the reported
53 mutations are truncating variants (Stamberger et al., 2016; Abramov et al., 2020),
54 haploinsufficiency is considered as the major disease mechanism, but a dominant-negative
55 mechanism has also been proposed for a subset of missense variants (Chai et al., 2016;
56 Guiberson et al., 2018). Several missense variants were modeled in *C. elegans*, and the mutant
57 worms show locomotion defects and increased convulsions in response to pentylenetetrazol
58 (Guiberson et al., 2018; Zhu et al., 2020). Haploinsufficiency was also modeled in fish and mice.
59 Removing *stxbp1b*, one of the two *STXBP1* homologs in zebrafish, causes spontaneous
60 electrographic seizures (Grone et al., 2016). The first three *Stxbp1* heterozygous knockout mouse
61 models recapitulated only a subset of neurological phenotypes seen in patients, possibly due to a
62 modest 25–50% reduction of Stxbp1 protein levels in these models (Hager et al., 2014;
63 Miyamoto et al., 2017; Kovačević et al., 2018; Orock et al., 2018). We recently generated two
64 new mouse *Stxbp1* null alleles, and the heterozygous mice ($Stxbp1^{tm1a/+}$ and $Stxbp1^{tm1d/+}$) show
65 50% reduction in Stxbp1 protein levels in most brain regions. The two new models recapitulated
66 nearly all features of *STXBP1* encephalopathy, as they show cognitive impairments, epileptic
67 seizures, motor dysfunction, developmental delay, anxiety-like behaviors, hyperactivity, and
68 aggression (Chen et al., 2020).
69

Mechanistically, how *STXBP1* heterozygous mutations lead to neurodevelopmental deficits remains elusive, even though it is well established that this protein is required for synaptic vesicle exocytosis in all neurons (Harrison et al., 1994; Verhage et al., 2000; Weimer et al., 2003; Grone et al., 2016), and its heterozygous null mutations impair synaptic transmission at both glutamatergic and GABAergic synapses (Toonen et al., 2006; Patzke et al., 2015; Orock et al., 2018; Miyamoto et al., 2019; Chen et al., 2020). As a first step to tackle this question, it is necessary to understand the roles of specific neurons, particularly glutamatergic and GABAergic neurons, in *STXBP1* encephalopathy pathogenesis. Furthermore, identifying the critical neuronal types can potentially provide therapeutic targets of disease. One study observed reduced survival and epileptiform discharges in GABAergic neurons-specific *Stxbp1* heterozygous knockout mice (Kovačević et al., 2018). However, other studies reported normal survival in a different line of GABAergic neurons-specific *Stxbp1* heterozygous knockout mice (Miyamoto et al., 2017) and instead observed spike-wave discharges in dorsal telencephalic glutamatergic neuron-specific heterozygous knockout mice (Miyamoto et al., 2019). Compared to the broad neurological and psychiatric impairments of *STXBP1* encephalopathy and *Stxbp1* haploinsufficient mice, the limited phenotypes of these cell type-specific *Stxbp1* heterozygous deletions seem to suggest that other neuronal types may be critical to the cognitive, motor, and psychiatric impairments. However, the efficacy and specificity of these *Stxbp1* conditional deletions were not confirmed. Thus, the significance of glutamatergic and GABAergic signaling to the disease pathogenesis is still unclear.

To address this question in a systematic manner, we generated and validated new glutamatergic and GABAergic neurons-specific *Stxbp1* haploinsufficient mice and determined their phenotypes

in the three core disease domains–cognitive impairment, epilepsy, motor dysfunction–as well as psychiatric functions and general health. Our comparative study reveals that together, glutamatergic and GABAergic *Stxbp1* haploinsufficiencient mice recapitulate the vast majority of the phenotypes observed in the constitutive haploinsufficient mice. However, GABAergic neurons mediate most of the neurodevelopmental phenotypes, whereas glutamatergic neurons are critical to a smaller, but different subset of phenotypes. These results support the notion that GABAergic synaptic dysfunction is a key mechanism shared among many neurodevelopmental disorders.

Results

Generation of glutamatergic or GABAergic neurons-specific *Stxbp1* haploinsufficient mice

To conditionally delete *Stxbp1* in mice, we crossed a previously generated *Stxbp1*$^{tm1a/+}$ mouse (Chen et al., 2020) with a Flp recombinase germline deleter mouse (see Materials and methods) to create a new *Stxbp1* flox allele (*tm1c*), in which exon 7 is flanked by two *loxP* sites (***Figure 1A***). Heterozygous (*Stxbp1*$^{f/+}$) and homozygous (*Stxbp1*$^{f/f}$) flox mice are viable and fertile. Western blots with antibodies recognizing either the N- or C-terminus of Stxbp1 showed that *Stxbp1*$^{f/+}$ and *Stxbp1*$^{f/f}$ mice had similar Stxbp1 protein levels to their wild type (WT) littermates at postnatal day 0 and 3 months of age (***Figure 1B*** and ***Figure 1-supplement 1***), indicating that the presence of *FRT* and *loxP* sites does not affect Stxbp1 expression. Deletion of exon 7 by Cre recombinase will lead to an early stop codon in exon 8 (***Figure 1A***), resulting in the same *Stxbp1 tm1d* null allele described previously (Chen et al., 2020).

To create *Stxbp1* haploinsufficiency selectively in glutamatergic neurons, we used a pan-

glutamatergic neuron-specific Cre line, *Vglut2-ires-Cre* (Vong et al., 2011). Vglut2 (vesicular glutamate transporter 2) is expressed in all glutamatergic neurons at embryonic and early postnatal stages (Boulland et al., 2004). Thus, Cre-mediated recombination occurs in all glutamatergic neurons. We crossed $Stxbp1^{f/+}$ mice with $Vglut2^{Cre/+}$ mice to obtain four genotypes: $Stxbp1^{+/+};Vglut2^{+/+}$ (WT), $Stxbp1^{f/+};Vglut2^{+/+}$ (Flox), $Stxbp1^{+/+};Vglut2^{Cre/+}$ (Vglut2-Cre), and $Stxbp1^{f/+};Vglut2^{Cre/+}$ (Vglut2-cHet). Similarly, we used a pan-GABAergic neuron-specific Cre line, *Vgat-ires-Cre* (Vong et al., 2011) to create *Stxbp1* haploinsufficiency selectively in GABAergic neurons. $Stxbp1^{f/+}$ mice were crossed with $Vgat^{Cre/+}$ mice to obtain $Stxbp1^{+/+};Vgat^{+/+}$ (WT), $Stxbp1^{f/+};Vgat^{+/+}$ (Flox), $Stxbp1^{+/+};Vgat^{Cre/+}$ (Vgat-Cre), and $Stxbp1^{f/+};Vgat^{Cre/+}$ (Vgat-cHet) (***Figure 1C***). All mice were on the C57BL/6J isogenic background.

To determine the efficiency and specificity of *Stxbp1* deletion in Vglut2-cHet and Vgat-cHet mice, we performed double fluorescent in situ hybridization (DFISH) to examine *Stxbp1* mRNA levels, as antibody staining cannot precisely identify the neuronal somas due to the presence of Stxbp1 in neurites (Ramos-Miguel et al., 2015). For Vglut2-cHet mice, we combined the probes against *Vglut1* and *Vglut2* to label all glutamatergic neurons with a single color. Compared to the three control groups (WT, Flox, and Vglut2-Cre), *Stxbp1* mRNA levels in Vglut2-cHet were reduced by 44–60% in glutamatergic neurons of most brain regions except cerebellar granular cells where the reduction was about 15–21% (***Figure 1D,F; Figure 1-supplement 2; Figure 1-supplement 3***). In contrast, *Stxbp1* mRNA levels in the *Vglut1* and *Vglut2*-negative neurons of the cortex, thalamic reticular nucleus (TRN), and striatum, which are mostly GABAergic neurons, were unaltered (***Figure 1D***; ***Figure 1-supplement 2A,B***; ***Figure 1-supplement***

3A,B,D). For Vgat-cHet mice, we used a probe against *Gad1* (glutamate decarboxylase 1) to label GABAergic neurons. *Stxbp1* mRNA levels in Vgat-cHet were reduced by 36–59% in GABAergic neurons of all brain regions (***Figure 1E,G; Figure 1-supplement 4***; ***Figure 1-supplement 5***). Furthermore, *Stxbp1* mRNA levels in the *Gad1*-negative neurons of the cortex, thalamus, and cerebellum, which are mostly glutamatergic neurons, were unaltered (***Figure 1E***; ***Figure 1-supplement 4A,B***; ***Figure 1-supplement 5A,C,D***). Thus, both *Vglut2-ires-Cre* and *Vgat-ires-Cre* efficiently and specifically deleted *Stxbp1* exon 7 and caused nonsense-mediated mRNA decay. These results demonstrate that Vglut2-cHet and Vgat-cHet are indeed glutamatergic and GABAergic neurons-specific *Stxbp1* haploinsufficient mice, respectively.

Guided by the phenotypes of constitutive haploinsufficient mice *Stxbp1*$^{tm1d/+}$ (Chen et al., 2020) and symptoms of *STXBP1* encephalopathy patients, we sought to characterize the neurological functions of male and female Vglut2-cHet and Vgat-cHet mice in comparison with their sex- and age-matched control littermates to dissect the contributions of glutamatergic and GABAergic neurons to *STXBP1* encephalopathy pathogenesis. We will conclude that glutamatergic or GABAergic neurons-specific *Stxbp1* haploinsufficiency significantly alters a phenotype only if Vglut2-cHet or Vgat-cHet mice, respectively, are statistically different from at least both Flox and Cre control mice.

GABAergic neurons-specific *Stxbp1* haploinsufficiency causes reduced survival, reduced body weight, dystonia, and impaired nesting behavior

Stxbp1$^{tm1d/+}$ mice show reduced survival and body weight, and develop dystonia that manifests as hindlimb stiffness or clasping (Chen et al., 2020). Thus, we monitored Vglut2-cHet, Vgat-cHet,

and their respective control mice weekly for their survival, body weight, and dystonia. Vglut2-cHet mice were observed at the expected Mendelian frequency (***Figure 2A,B***), and they had a normal survival rate when monitored up to one year (***Figure 2C,D***). Vgat-cHet mice were also observed at the expected Mendelian frequency at postnatal day 14 (***Figure 2A***), but about 20% of them died during postnatal weeks 3 and 4 (***Figure 2B***), indicating a postnatal lethality phenotype. Interestingly, those Vgat-cHet mice that survived through this period had a similar survival rate as control mice (***Figure 2C,D***). The partially penetrant lethality phenotype of Vgat-cHet mice is similar that of *Stxbp1*$^{tm1d/+}$ mice (Chen et al., 2020).

While the body weight of Vglut2-cHet mice was indistinguishable from that of their sex- and age-matched control littermates (***Figure 2E***), Vgat-cHet mice were smaller and weighted about 9% less than control mice (***Figure 2F***). Furthermore, both Vglut2-cHet and Vgat-cHet mice began to develop dystonia around 3–4 weeks of age and progressively exacerbated over the next month (***Figure 2G,H***). The dystonia of Vgat-cHet mice was much more severe than that of Vglut2-cHet mice. By the age of 6 months, 78% Vgat-cHet mice developed hindlimb clasping, but only 24% Vglut2-cHet mice did (***Figure 2I***).

To further assess mouse well-being, we examined the innate nest building behavior by providing a Nestlet (pressed cotton square) to each mouse in the home cage and scoring the degree of shredding and nest quality after 24 hours (***Figure 2J,K***). Vgat-cHet mice built worse nests than control mice, similar to *Stxbp1*$^{tm1d/+}$ mice (Chen et al., 2020), whereas Vglut2-cHet mice were normal (***Figure 2K***).

Altogether, these results show that *Stxbp1* haploinsufficiency in GABAergic neurons alone is sufficient to recapitulate the reduced survival, smaller body weight, dystonia, and impaired nesting behavior observed in the constitutive *Stxbp1* haploinsufficient mice.

Increased anxiety-like behaviors and hyperactivity of GABAergic neurons-specific *Stxbp1* haploinsufficient mice

Anxiety was reported in a subset of *STXBP1* encephalopathy patients (Marchese et al., 2016; Suri et al., 2017), and several lines of constitutive *Stxbp1* heterozygous knockout mice including *Stxbp1*$^{tm1d/+}$ show increased anxiety (Hager et al., 2014; Miyamoto et al., 2017; Kovačević et al., 2018; Chen et al., 2020). Thus, we used the elevated plus maze test to assess anxiety-like behaviors. Vgat-cHet mice entered the open arms less frequently, spent less time, and traveled shorter distance in the open arms than control mice (***Figure 3A–C***), but their activities in the closed arms were largely normal (***Figure 3D***), showing the heightened anxiety of Vgat-cHet mice. In contrast, Vglut2-cHet mice did not show increased anxiety-like behaviors in this test (***Figure 3A–D***).

We next used the open-field test to examine mouse locomotion, exploration, and anxiety-like behaviors, as *Stxbp1*$^{tm1d/+}$ mice show hyperactivity and increased anxiety-like behaviors in this test (Chen et al., 2020). Typically, the activities of mice decrease over time in this test, as mice become acclimated to the test arena. The locomotion of Vglut2-cHet mice was similar to that of control mice (***Figure 3E,F***). In contrast, Vgat-cHet mice showed a hyperactive phenotype, as their activities did not decrease over time and they traveled longer distances and faster than control mice in the later phase of the test (***Figure 3E,F***). Vgat-cHet mice explored the center

region of the arena less than control mice (***Figure 3G***), consistent with their heightened anxiety. Interestingly, we observed that Vglut2-cHet mice also avoided the arena center region and made fewer vertical movements (***Figure 3G,H***), indicating an increase in anxiety as well.

We also performed marble burying test to evaluate innate digging behavior. The numbers of marbles buried by Vglut2-cHet or Vgat-cHet mice were not statistically different from those of the control mice, even though Vgat-cHet mice buried fewer marbles (***Figure 3-supplement 1A***). Taken the results of the elevated plus maze and open-field tests together, both glutamatergic and GABAergic neurons contribute to anxiety-like behaviors with GABAergic neurons being more critical, as elevated plus maze test is a more specific assay for anxiety-like behaviors in mice. Furthermore, *Stxbp1* haploinsufficiency in GABAergic neurons mediates the hyperactivity phenotype of constitutive *Stxbp1* haploinsufficient mice.

Impaired motor coordination and normal sensory functions of GABAergic neurons-specific *Stxbp1* haploinsufficient mice

We next evaluated motor functions using rotarod, vertical pole, and footslip tests, as motor deficits are prevalent in *STXBP1* encephalopathy patients (Stamberger et al., 2016) and were observed in *Stxbp1*$^{tm1d/+}$ mice (Chen et al., 2020). We performed rotarod test for 4 consecutive days to evaluate motor learning and coordination by measuring the latency of mice to fall from a rotating rod. Vglut2-cHet mice performed similarly to control mice except the first trial where they fell off the rotating rod earlier (***Figure 3-supplement 2B***), whereas Vgat-cHet mice stayed longer on the rod than control mice across multiple trials (***Figure 3-supplement 2C***), probably

due to their smaller body weight (***Figure 2F***) and hyperactivity (***Figure 3E,F***). This rotarod phenotype of Vgat-cHet mice is similar to that of *Stxbp1*$^{tm1d/+}$ mice (Chen et al., 2020).

The vertical pole test assesses the agility of mice by measuring the amount of time it takes for mice to descend from the top of a vertical pole. Vgat-cHet mice took 80% more time to complete this task than control mice (***Figure 3I***). When allowed to walk on a wire grid, Vgat-cHet mice had difficulty in placing their paws precisely on the wire to hold themselves and slipped 85–97% more frequently than control mice (***Figure 3J***). In contrast, Vglut2-cHet mice performed normally in both vertical pole and footslip tests (***Figure 3I,J***). Together, these results show that like constitutive *Stxbp1* haploinsufficient mice, Vgat-cHet mice do not develop ataxia, but their fine motor coordination is impaired.

Finally, both Vglut2-cHet and Vgat-cHet mice showed normal acoustic startle responses (***Figure 3-supplement 2A***), pre-pulse inhibition (***Figure 3-supplement 2B***), and thermal nociception (***Figure 3-supplement 2C***). Since *Stxbp1*$^{tm1d/+}$ mice are normal in these tests too, these results indicate that glutamatergic or GABAergic neurons-specific *Stxbp1* haploinsufficiency does not lead to additional abnormalities in sensory functions and sensorimotor gating.

Social aggression is increased in GABAergic neurons-specific *Stxbp1* haploinsufficient mice

A subset of *STXBP1* encephalopathy patients exhibit autistic features and aggressive behaviors (Stamberger et al., 2016; Abramov et al., 2020). *Stxbp1*$^{tm1d/+}$ mice show normal social interactions in the three-chamber test, but male resident *Stxbp1*$^{tm1d/+}$ mice exhibit elevated innate aggression towards male intruder mice in the resident-intruder test (Chen et al., 2020). Thus, we

evaluated Vglut2-cHet and Vgat-cHet mice in these two tests. In the three-chamber test, both Vglut2-cHet and Vgat-cHet mice preferred to interact with a sex- and age-matched partner mouse rather than an object, similar to the control mice (***Figure 4A***), showing their normal sociability. In the resident-intruder test, male resident Vgat-cHet mice started the first attack sooner, initiated more attacks, and spent more time attacking the intruders than control mice (***Figure 4B–E***), all of which indicate an elevated innate aggression. In contrast, Vglut2-cHet mice were not statistically different from control mice in any of these parameters, although there might be signs of elevated aggression based on the number of attacks and total duration of attacks (***Figure 4B–E***). These results indicate that GABAergic neurons are critically involved in the elevated innate aggression caused by *Stxbp1* haploinsufficiency.

Glutamatergic and GABAergic neurons-specific *Stxbp1* haploinsufficiencies differentially impair cognitive functions

One of the core features of *STXBP1* encephalopathy is intellectual disability (Stamberger et al., 2016; Abramov et al., 2020), which is recapitulated by the severe cognitive deficits in *Stxbp1*$^{tm1d/+}$ mice (Chen et al., 2020). Thus, we assessed the cognitive functions of Vglut2-cHet and Vgat-cHet mice. We first performed the novel object recognition test, in which WT mice prefer to explore a novel object over a familiar object, whereas *Stxbp1*$^{tm1d/+}$ mice fails to recognize the novel object (Chen et al., 2020). Surprisingly, neither Vglut2-cHet nor Vgat-cHet mice showed a deficit in this test (***Figure 5A; Figure 5-supplement 1***). This result was unexpected because novel object recognition is thought to depend on the hippocampus and cortex (Antunes and Biala, 2012; Cohen and Stackman, 2015), and *Stxbp1* haploinsufficiency impairs GABAergic synaptic transmission in the cortex (Chen et al., 2020), which is expected to

alter cortical functions in Vgat-cHet mice. Vgat-cHet mice so far have recapitulated most of the phenotypes of *Stxbp1*$^{tm1d/+}$ mice. Thus, the intact recognition memories in Vglut2-cHet and Vgat-cHet mice indicate that *Stxbp1* haploinsufficiency in glutamatergic or GABAergic neurons alone is not sufficient to impair novel object recognition or other neuronal types are more important for this cognitive function.

To further examine cognitive functions by another test, we evaluated Vglut2-cHet and Vgat-cHet mice in the Pavlovian fear conditioning paradigm, in which *Stxbp1*$^{tm1d/+}$ mice display a strong reduction in both context- and cue-induced freezing behaviors 24 hours after conditioning (Chen et al., 2020). Interestingly, Vglut2-cHet and Vgat-cHet mice showed a selective deficit in hippocampus-independent cued fear memory and hippocampus-dependent contextual fear memory, respectively (***Figure 5B,C***). Vglut2-cHet mice were normal in contextual memory (***Figure 5B***), whereas Vgat-cHet mice even had slightly better cued memory than control mice (***Figure 5C***). The reduced freezing responses in Vglut2-cHet and Vgat-cHet mice were not due to sensory dysfunctions as their acoustic startle responses and nociception were intact (***Figure 3-supplement 3A,C***). This striking segregation of two forms of associative memory in Vglut2-cHet and Vgat-cHet mice highlights the importance of both glutamatergic and GABAergic neurons in the cognitive deficits of *STXBP1* encephalopathy.

Distinct epileptic seizures in glutamatergic and GABAergic neurons-specific *Stxbp1* haploinsufficient mice

Epilepsy is a hallmark feature of *STXBP1* encephalopathy and patients present diverse types including epileptic spasm, focal, tonic, clonic, myoclonic, and absence seizures (Stamberger et

al., 2016; Suri et al., 2017). Constitutive *Stxbp1* heterozygous knockout mice including *Stxbp1*$^{tm1d/+}$ mice have frequent spike-wave discharges (SWDs) and myoclonic seizures that manifested as involuntary muscle jerks associated with EEG discharges or sudden jumps (Kovačević et al., 2018; Miyamoto et al., 2019; Chen et al., 2020). We performed chronic video-electroencephalography (EEG) and electromyography (EMG) recordings in freely moving Vglut2-cHet, Vgat-cHet, and control mice (***Figure 6A–C***). All Vglut2-cHet mice exhibited numerous spike-wave discharges (SWDs), which is similar to *Stxbp1*$^{tm1d/+}$ mice (***Figure 6B,D; Video 1***). This result is also consistent with the report that heterozygous deletion of *Stxbp1* in dorsal telencephalic glutamatergic neurons caused frequent SWDs (Miyamoto et al., 2019). The myoclonic jerks and jumps of Vglut2-cHet mice were indistinguishable from those of control mice (***Figure 6E,G***). In contrast, Vgat-cHet mice did not show frequent SWDs (***Figure 6D***), but all had many myoclonic jerks and jumps, particularly during rapid eye movement (REM) and non-rapid eye movement (NREM) sleeps (***Figure 6C,E–G; Video 2; Video 3***). Thus, the segregation of two types of seizures in Vglut2-cHet and Vgat-cHet mice again highlights the important, but different, roles of glutamatergic and GABAergic neurons in the epileptogenesis for *STXBP1* encephalopathy.

Discussion

Glutamatergic and GABAergic neurons together mediate most of the neurological impairments of *STXBP1* encephalopathy. Vgat-cHet mice exhibit reduced body weight, early lethality, hindlimb clasping, motor dysfunction, impaired nest building, hyperactivity, aggression, impaired contextual fear memory, and myoclonic seizures, whereas Vglut2-cHet mice show impaired cued fear memory and SWDs. Only the impaired marble burying and novel object

recognition of constitutive *Stxbp1* haploinsufficient mice are not recapitulated by either Vglut2-cHet or Vgat-cHet mice (***Figure 7***; ***Supplementary File 2***). Thus, it is likely that glutamatergic and especially GABAergic neurons are the most critical cell types to *STXBP1* encephalopathy. It would be worth determining to what extent the neurodevelopmental deficits of constitutive *Stxbp1* haploinsufficient mice can be rescued by restoring *Stxbp1* expression solely in GABAergic neurons. We previously observed two deficits of cortical inhibition in constitutive *Stxbp1* haploinsufficient mice – a reduction in the synaptic strength of parvalbumin-expressing interneurons and a reduction in the connectivity of somatostatin-expressing interneurons (Chen et al., 2020). It would be interesting to determine the specific contribution of each of these two main classes of GABAergic neurons to the disease pathogenesis. Future experiments are also necessary to determine if other neurotransmitter systems such as dopaminergic and noradrenergic neurons are important, particularly for object recognition memory.

GABAergic *Stxbp1* haploinsufficiency overall causes substantially broader and more severe phenotypes than glutamatergic *Stxbp1* haploinsufficiency (***Figure 7***; ***Supplementary File 2***), supporting the notion that reduced inhibition is a primary mechanism of *STXBP1* encephalopathy (Chen et al., 2020). This is in sharp contrast with previous studies that indicate a major role of impaired excitatory synaptic transmission in the disease pathogenesis (Patzke et al., 2015; Miyamoto et al., 2017; Orock et al., 2018; Miyamoto et al., 2019), in part because previous models of heterozygous deletion of *Stxbp1* in GABAergic neurons revealed few phenotypes. The first model using an *Stxbp1* exon 3-floxed allele and a bacterial artificial chromosome transgenic *Vgat-Cre* line resulted in normal survival, locomotion, fear memory, and innate aggression (Miyamoto et al., 2017). The second model using an *Stxbp1* exon 2-floxed allele and a *Gad2*-

345 *ires-Cre* line showed partial early lethality, but other neurological functions were not studied
346 (Kovačević et al., 2018). Both models had epileptiform activities that are likely the same
347 myoclonic seizures of our model, but the lack of quantitative characterization precludes a
348 comparison with our results in detail (Kovačević et al., 2018; Miyamoto et al., 2019). Apart from
349 different experimental conditions or assays that may have contributed to the difference among
350 studies, one possible difference among these models is the efficiency and specificity of *Stxbp1*
351 deletion due to different *Cre* lines and recombination efficacies of different *Stxbp1* flox alleles,
352 as previous studies did not validate the genetic manipulations like what we did. Since there are
353 milder phenotypes and Stxbp1 protein reductions in the constitutive *Stxbp1* heterozygous
354 knockout mice derived from the two previous flox alleles than our *Stxbp1* flox allele-derived
355 $Stxbp1^{tm1d/+}$ mice (Miyamoto et al., 2017; Kovačević et al., 2018; Chen et al., 2020), different
356 levels of Stxbp1 protein reduction in different *Stxbp1* flox alleles-mediated deletions may also
357 contribute to the phenotypic differences. Furthermore, we studied Vglut2-cHet and Vgat-cHet
358 mice in parallel and with much larger cohorts of mice than previous studies, allowing a better
359 detection and comparison of neurodevelopmental phenotypes.
360
361 Glutamatergic and GABAergic neurons are extensively interconnected throughout the brain, and
362 their synaptic interactions control the spatiotemporal patterns of neuronal activity and brain
363 functions. Thus, one would expect that manipulating a gene that is important for both
364 glutamatergic and GABAergic neurons in either neuronal type should lead to largely overlapping
365 neurological phenotypes. For instance, deletion of Rett syndrome gene *Mecp2* (*methyl-CpG-*
366 *binding protein 2*) in glutamatergic or GABAergic neurons causes many common phenotypes in
367 mice (Gemelli et al., 2006; Chao et al., 2010; Meng et al., 2016). On the contrary, our cell type-

specific deletion studies reveal distinct roles of these two neuronal types in the phenotypic spectrum of *STXBP1* encephalopathy. The only shared phenotypes between Vglut2-cHet and Vgat-cHet mice are dystonia and increased anxiety-like behaviors (***Figure 7***; ***Supplementary File 2***). Intriguingly, glutamatergic and GABAergic neurons each independently subserves one of the two forms of associative memories in Pavlovian fear conditioning and one of the two seizure types. This unexpected phenotypic segregation between excitatory and inhibitory neurons suggests that different neurological functions exhibit different susceptibilities to the presynaptic dysfunction caused by *Stxbp1* haploinsufficiency in glutamatergic or GABAergic neurons. The distinct roles of glutamatergic and GABAergic neurotransmitter systems in *STXBP1* encephalopathy present both challenges and opportunities for therapeutic interventions. Both neuronal types should be the primary targets, but their wide distribution throughout the brain makes it difficult for gene-based therapies such as adeno-associated virus-mediated gene replacement to achieve a high degree of coverage for both populations. On the other hand, the clinical symptoms vary considerably among patients, and some patients present only a subset of disease phenotypes. Thus, modulating one of these two neurotransmitter systems by small molecules such as transmitter receptor modulators may allow more precise treatment of the symptoms.

The reduction of glutamatergic and GABAergic synaptic transmission caused by *STXBP1* or *Stxbp1* heterozygous mutations are rather modest (Toonen et al., 2006; Patzke et al., 2015; Orock et al., 2018; Miyamoto et al., 2019; Chen et al., 2020), yet the neurological impairments in humans and mice are severe (Stamberger et al., 2016; Abramov et al., 2020; Chen et al., 2020), highlighting the profound impacts of subtle presynaptic dysfunctions on neuronal functions.

STXBP1 encephalopathy shares the core clinical features with other synaptic vesicle cycle disorders, including intellectual disability, epilepsy, and motor dysfunctions. Thus, understanding the cellular and circuit origins of this disorder provides mechanistic insights into the growing list of neurodevelopmental disorders caused by presynaptic dysfunctions.

Materials and Methods

Mice

Stxbp1 flox mice were generated from a previously described *Stxbp1* knockout-first allele (*tm1a*) that contains a trapping cassette flanked by two *FRT* sites and the exon 7 flanked by two *loxP* sites (Chen et al., 2020). $Stxbp1^{tm1a/+}$ mice were crossed to *Rosa26-Flpo* mice (JAX #012930)(Raymond and Soriano, 2007) to remove the trapping cassette in the germline, resulting in the *Stxbp1* flox allele (*tm1c*). *Stxbp1* flox mice were genotyped by PCR using a pair of primers 5'-TTCCACAGCCCTTTACAGAAAGG-3' and 5'-ATGTGTATGCCTGGACTCACAGGG-3' for both WT (352 bp) and *tm1c* (500 bp) alleles. *Stxbp1* flox mice were maintained on the C57BL/6J background by crossing to WT C57BL/6J mice (JAX # 000664). Heterozygous *Stxbp1* flox female mice ($Stxbp1^{f/+}$) were crossed with C57BL/6J-congenic heterozygous *Vglut2-ires-Cre* (JAX # 028863)(Vong et al., 2011) male mice to generate $Stxbp1^{f/+};Vglut2^{Cre/+}$, $Stxbp1^{f/+};Vglut2^{+/+}$, $Stxbp^{+/+}$, $Vglut2^{cre/+}$, and WT mice. $Stxbp1^{f/+}$ female mice were also crossed with C57BL/6J-congenic heterozygous *Vgat-ires-Cre* (JAX # 028862)(Vong et al., 2011) male mice to generate $Stxbp1^{f/+};Vgat^{Cre/+}$, $Stxbp1^{f/+}$, $Vgat^{+/+}$, $Stxbp1^{+/+}$, $Vgat^{Cre/+}$, and WT mice. Male white BALB/cAnNTac mice (Taconic # BALB-M) or BALB/cJ (JAX # 000651) were used for the resident-intruder test. Mice were housed in an Association for Assessment and Accreditation of Laboratory Animal Care International-certified animal facility on a 14-hour/10-hour light/dark

414 cycle. All procedures to maintain and use mice were approved by the Institutional Animal Care
415 and Use Committee at Baylor College of Medicine.
416
417 **Western blots**
418 Western blot analyses were performed according to the protocols published previously (Chen et
419 al., 2020) with minor modifications. Proteins were extracted from the entire mouse brains on
420 postnatal day 0 or the cortices from 3-month-old mice. The lysis buffer contained 50 mM Tris-
421 HCl (pH 7.6), 150 mM NaCl, 1 mM EDTA, 1% Triton X-100, 0.5% Na-deoxycholate, 0.1%
422 SDS, and 1 tablet of cOmplete™, Mini, EDTA-free Protease Inhibitor Cocktail (Roche, catalog #
423 SKU 11836170001) in 10 ml buffer. Stxbp1 was detected by a rabbit antibody against the N
424 terminal residues 58–70 (Abcam, catalog # ab3451, lot #GR79394-18, 1:2,000 or 1:5,000
425 dilution) or a rabbit antibody against the C terminal residues 580–594 (Synaptic Systems, catalog
426 # 116002, lot # 116002/15, 1:2,000 or 1:5,000 dilution). Gapdh was detected by a rabbit antibody
427 (Santa Cruz Biotechnology, catalog # sc-25778, lot # A0515, 1:300 or 1:1,000 dilution). Primary
428 antibodies were detected by a goat anti-rabbit antibody conjugated with IRDye 680LT (LI-COR
429 Biosciences, catalog # 925-68021, lot # C40917-01, 1:20,000 dilution). Proteins were visualized
430 and quantified using an Odyssey CLx Imager and Image Studio Lite version 5.0 (LI-COR
431 Biosciences). Stxbp1 levels were normalized by the Gapdh levels. Each mouse was tested by
432 both Stxbp1 antibodies and the results from the two antibodies were averaged.
433
434 **Double fluorescent *in situ* hybridization and imaging**
435 A digoxigenin (DIG)-labeled RNA antisense probe against mouse *Stxbp1* and fluorescein
436 (FITC)-labeled RNA antisense probes against mouse *Vglut1* (*Slc17a7*), *Vglut2* (*Slc17a6*), or

437 *Gad1* were generated by *in vitro* transcription using cDNA templates and RNA DIG- or FITC-
438 labeling kits (Sigma, catalog # 11277073910 or 11685619910, respectively). The DNA templates
439 were made by PCR amplification from a plasmid pCMV-SPORT6-Stxbp1a (GenBank:
440 BC031728.1, Transomic Technologies) for the *Stxbp1* probe or from mouse brain cDNA for the
441 *Vglut1*, *Vglut2*, and *Gad1* probes, with a SP6 promoter (ATTTAGGTGACACTATAG) or a T3
442 promoter (AATTAACCCTCACTAAAGGG) added at the 5' end of the PCR forward primers
443 and a T7 promoter (TAATACGACTCACTATAGGG) at the 5' end of the PCR reverse primers.
444 The sequences of *Stxbp1*, *Vglut1*, and *Vglut2* probes were from Allen Brain Atlas
445 (http://mouse.brain-map.org) and *Gad1* from Eurexpress (http://www.eurexpress.org/ee/). The
446 probe sequences are listed in the ***Supplementary File 1***.
447
448 Double fluorescent *in situ* hybridization (DFISH) was performed by the RNA *In Situ*
449 Hybridization Core at Baylor College of Medicine using an automated robotic platform and
450 procedures as described previously (Yaylaoglu et al., 2005) with minor modifications for double
451 ISH. Briefly, fresh-frozen brains were embedded in optimal cutting temperature (OCT)
452 compound and cryosectioned (25 µm). Two or three probes were hybridized to brain sections
453 simultaneously (*Stxbp1*/*Gad1* or *Stxbp1*/*Vglut1*/*Vglut2*) in hybridization buffer (Ambion, catalog
454 # B8807G). Sections were washed with standard saline citrate stringency solution (SSC; 0.15 M
455 NaCl, 0.015 M sodium citrate) to remove unbound and non-specifically bound probes. To
456 visualize the DIG-labeled probe, brain sections were incubated for 30 minutes with a horse
457 radish peroxidase (HRP)-conjugated sheep anti-DIG primary antibody (Sigma, catalog #
458 11207733910) diluted at 1/500 in Tris-NaCl blocking buffer (TNB; 100 mM Tris, 150 mM
459 NaCl, 0.5% (w/v) blocking reagent (Perkin Elmer, catalog # FP1012), pH 7.6). After washes in

Tris-NaCl-Tween (TNT; 10 mM Tris-HCl, pH 8.0, 150 mM NaCl and 0.05% TWEEN 20) buffer, brain sections were then developed with tyramide-Cy3 Plus (Akoya Biosciences, catalog # NEL744001KT, 1/50 dilution in amplification diluent, 15 minutes). After washes in TNT buffer, the remaining HRP activity was quenched by a 10-minute incubation in 0.2 M HCl. Sections were then washed in TNT, blocked in TNB for 15 minutes before incubation with an HRP-conjugated sheep anti-FITC antibody (Sigma, catalog # 11426346910) diluted at 1/500 in TNB for 30 minutes. After washes in TNT, the FITC-labeled probe was visualized using tyramide-FITC Plus (Akoya Biosciences, catalog # NEL741001KT, 1/50 dilution in amplification diluent, 15 minutes). The slides were washed in TNT and stained with 4',6-diamidino-2-phenylindole (DAPI; Invitrogen, catalog # D3571), washed again, removed from the machine, and mounted in ProLong Diamond (Invitrogen, catalog # P36961).

Vglut2-cHet or Vgat-cHet and their respective control mice were processed, and brain sections were stained and imaged in parallel. Fluorescent images of brain sections were acquired using an Axio Zoom.V16 fluorescence microscope (Zeiss) and processed using Imaris (Oxford Instruments) or ImageJ (National Institutes of Health). The frontal cortex, somatosensory cortex, hippocampus, thalamus, reticular thalamic nucleus, striatum, and cerebellum were analyzed from sagittal sections, and amygdala and hypothalamus from coronal sections. 3–8 sections from each mouse were analyzed for each brain region. For *Vglut1/2*- or *Gad1*-positive cells, individual somas were selected using the surface function of Imaris with the following parameters: surface detail = 0.811, diameter of the largest square = 25 μm for cortical pyramidal neurons and Purkinje cells, and 20 μm for other neurons; pixels with the intensity at the lower 2–4% range of the maximal intensity were removed; voxels with the size at the lower 1.5–2% range of the

maximal voxel size was removed. The mean intensity of *Stxbp1* was measured in each of the selected somas and then the average intensity was calculated across all selected cells for a brain section. For *Vglut1/2*- or *Gad1*-negative cells, *Vglut1/2*- or *Gad1*-positive cells were first selected as described above and removed. Individual *Vglut1/2*- or *Gad1*-negative somas were then selected based on *Stxbp1* signals using the parameters described above. The mean intensity of *Stxbp1* was measured in each of the selected somas and the average intensity was calculated across all selected cells for a brain section. Approximately 200–600 *Vglut1/2*-positive or *Gad1*-negative cells and 50–100 *Gad1*-positive or *Vglut1/2*-negative cells were selected for a brain region except the striatum where about 800 cells were selected in each section. For the hippocampal pyramidal neurons and cerebellar granular cells, due to their high cellular densities, the soma region of a group cells instead of individual cells was selected manually and the mean *Stxbp1* intensities were measured using ImageJ. Background signals were measured in intercellular space and subtracted from each measurement. *Stxbp1* levels from different brain sections were normalized by the average *Stxbp1* levels of WT brain sections that were simultaneously stained and imaged.

Health monitoring

Body weight and dystonia of mice were monitored weekly. Dystonia was assessed by holding mice on their tails briefly in air and observing the movement of hindlimbs. Dystonia was scored as 0 = no dystonia, 1 = stiffness in hindlimb, 2 = clasping of one hindlimb, 3 = clasping of both hindlimbs, 4 = tight clasping of both hindlimbs.

Behavioral tests

All behavioral experiments were performed using the equipment and facility at the Neurobehavioral Core of Baylor College of Medicine Intellectual and Developmental Disabilities Research Center. All tests were performed and analyzed blind to the genotypes according to the protocols published previously (Chen et al., 2020) with minor modifications. Approximately equal numbers of cHet mice and their sex- and age-matched WT, Flox and Cre littermates were tested in parallel in each experiment except for resident intruder test where only male mice were used. Mice were habituated in the behavioral test facility for at least 30 minutes before testing. The sexes and ages of the tested mice were indicated in the figures.

Nesting test: An autoclaved Nestlet was given to a mouse individually housed in its home cage, and the quality of the nest was scored after 24 hours.

Elevated plus maze test: A mouse was placed in the center of an elevated maze consisting of two open arms (25 × 8 cm) and two closed arms with high walls (25 × 8 × 15 cm). The mouse was initially placed facing the open arms and then allowed to freely explore for 10 minutes with 150–200-lux illumination and 65-dB background white noise. The mouse activity was recorded using a video camera (ANY-maze, Stoelting).

Open-field test: A mouse was placed at the center of a clear, open chamber (40 × 40 × 30 cm) and allowed to freely explore for 30 minutes with 150–200-lux illumination and 65-dB background white noise. The horizontal plane was evenly divided into 256 squares (16 × 16), and the center zone is defined as the central 100 squares (10 × 10). The horizontal travel and vertical activity were quantified by either an Open Field Locomotor system or a VersaMax

system (OmniTech).

Marble burying test: A clean standard housing cage was filled with approximately 8-cm deep bedding material. 20 marbles were arranged on top of the bedding in a 4 × 5 array. A mouse was placed into this cage for 30 minutes before the number of buried marbles (i.e., at least 50% of the marble covered by the bedding material) was recorded.

Rotarod test: A mouse was tested on an accelerating rotarod apparatus (Ugo Basile) in 3 trials per day for 4 consecutive days. There was a 30–60-minute resting interval between trials. Each trial lasted for a maximum of 5 minutes, during which the rod accelerated linearly from 4 to 40 revolutions per minute (RPM). The time when the mouse walks on the rod and the latency for the mouse to fall from the rod were recorded for each trial.

Foot slip test: A mouse was placed onto an elevated 40 × 25 cm wire grid (1 × 1 cm spacing) and allowed to freely move for 5 minutes. The number of foot slips was manually counted, and the moving distance was measured through a video camera (ANY-maze, Stoelting). The number of foot slips were normalized by the moving distance for each mouse.

Vertical pole test: A mouse was placed at the top of a vertical threaded metal pole (1.3-cm diameter, 55-cm length). The amount of time for the mouse to descend to the floor was measured with a maximal cutoff time of 120 seconds.

Acoustic startle response test: A mouse was placed in a plastic cylinder and acclimated to the 70-

552 dB background white noise for 5 minutes. The mouse was then tested with 4 blocks, and one
553 block consisted of 13 trials. In one block, each of 13 different levels of sound (70, 74, 78, 82, 86,
554 90, 94, 98, 102, 106, 110, 114, or 118 dB, 40 ms, inter-trial interval of 15 seconds on average)
555 was presented in a pseudorandom order. The startle response was recorded for 40 ms after the
556 onset of the sound. The rapid force changes due to the startles were measured by an
557 accelerometer (SR-LAB, San Diego Instruments).
558
559 Pre-pulse inhibition test: A mouse was placed in a plastic cylinder and acclimated to the 70 dB
560 background noise for 5 minutes. The mouse was then tested with 6 blocks, and one block
561 consisted of 8 trials in a pseudorandom order: a "no stimulus" trial (40 ms, only 70 dB
562 background noise present), a test pulse trial (40 ms, 120 dB), 3 different pre-pulse trials (20 ms,
563 74, 78, or 82 dB), and 3 different pre-pulse inhibition trials (a 20 ms, 74, 78, or 82 dB pre-pulse
564 preceding a 40 ms, 120 dB test pulse by 100 ms). The startle response was recorded for 40 ms
565 after the onset of the 120 dB test pulse. The inter-trial interval is 15 s on average. The rapid force
566 changes due to the startles were measured by an accelerometer (SR-LAB, San Diego
567 Instruments). Pre-pulse inhibition of the startle responses was calculated as “1 – (pre-pulse
568 inhibition trial/test pulse trial)”.
569
570 Hot plate test: A mouse was placed on a hot plate (Columbus Instruments) with a temperature of
571 55 °C. The latency for the mouse to first respond with either a hind paw lick, hind paw flick, or
572 jump was recorded. If the mouse did not respond within 45 seconds, then the test was terminated,
573 and the latency was recorded as 45 seconds.
574

Three-chamber test: The apparatus (60.8 × 40.5 × 23 cm) consists of three chambers (left, center, and right) of equal size with 10 × 5 cm openings between the chambers. A test mouse was placed in the apparatus with a mesh pencil cup in each of the left and right chambers and allowed to freely explore for 10 minutes. A novel object was then placed under one mesh pencil cup and an age- and sex-matched partner mouse (WT C57BL/6J) under the other mesh pencil cup. The test mouse was allowed to freely explore for another 10 minutes. The position of the test mouse was tracked through a video camera (ANY-maze, Stoelting), and the approaches of the test mouse to the object or partner mouse were scored manually. Partner mice were habituated to the mesh pencil cups in the apparatus for 1 hour per day for 2 days prior to testing. A partner mouse was used only in one test per day.

Resident-intruder test: Male test mice (resident mice) were individually caged for 2 weeks before testing. Age-matched male BALB/cAnNTac or BALB/cJ mice were group-housed to serve as the intruders. During the test, an intruder was placed into the home cage of a test mouse for 10 minutes, and their behaviors were video recorded. Videos were scored for the number and duration of each attack by the resident mouse regardless the attack was initiated by either the resident or intruder.

Novel object recognition test: A mouse was first habituated in an empty arena (24 × 45 × 20 cm) for 5 minutes before every trial, and then placed into the testing arena with two identical objects (i.e., familiar object 1 and familiar object 2) for the first three trials. In the fourth trial, familiar object 1 was replaced with a novel object. In the fifth trial, the mouse was presented with the two original, identical objects again. Each trial lasted 5 minutes. The inter-trial interval was 24 hours.

598 The movement of mice was recorded by a video camera. The amount of time that the mouse
599 interacted with the objects (*T*) was recorded using a wireless keyboard (ANY-maze, Stoelting).
600 The preference index of interaction was calculated as $T_{familiar\ object\ 1}/(T_{familiar\ object\ 1} + T_{familiar\ object\ 2})$
601 for the first three trials and fifth trial and as $T_{novel\ object}/(T_{novel\ object} + T_{familiar\ object\ 2})$ for the fourth
602 trial.
603
604 Fear conditioning test: Pavlovian fear conditioning was conducted in a chamber (30 × 25 × 29
605 cm) with a grid floor for delivering electrical shocks (Coulbourn Instruments). During the 5-
606 minute training phase, a mouse was placed in the chamber for 2 minutes, and then a sound (85
607 dB, white noise) was turned on for 30 seconds immediately followed by a mild foot shock (2 sec,
608 0.72 mA). The same sound and foot shock were repeated one more time 2 minutes after the first
609 foot shock. After the second foot shock, the mouse stayed in the training chamber for 18 seconds
610 before returning to its home cage. After 24 hours, the mouse was tested for the contextual and
611 cued fear memories. In the contextual fear test, the mouse was placed in the same training
612 chamber and its freezing behavior was monitored for 5 minutes without the sound stimulus. The
613 mouse was then returned to its home cage. One to two hours later, the mouse was transferred to
614 the chamber after it has been altered using plexiglass inserts and a different odor to create a new
615 context for the cued fear test. After 3 minutes in the chamber, the same sound cue that was used
616 in the training phase was turned on for 3 minutes without foot shocks while the freezing behavior
617 was monitored. The freezing behavior was scored using an automated video-based system
618 (FreezeFrame, Actimetrics). The freezing time (%) during the first 2 minutes of the training
619 phase (i.e., before the first sound) was subtracted from the freezing time (%) during the
620 contextual fear test. The freezing time (%) during the first 3 minutes of the cued fear test (i.e.,

without sound) was subtracted from the freezing time (%) during the last 3 minutes of the cued fear test (i.e., with sound).

Video-EEG/EMG

Video-EEG/EMG recordings and analysis were performed as previously described (Chen et al., 2020). Briefly, mice at 8–13 weeks of age were anesthetized with 2.5% isoflurane in oxygen. Approximately 0.25 mm-diameter craniotomies were performed at the coordinates below that were normalized by the distance between bregma and lambda (DBL). Perfluoroalkoxy polymer (PFA)-coated silver wire electrodes (A-M Systems, catalog # 786000, 127 mm bare diameter, 177.8 mm coated diameter) were used for grounding at the right frontal cortex, referencing at the cerebellum, and recording at the left frontal cortex (anterior posterior (AP): 0.42 of DBL, medial lateral (ML): 0.356 of DBL, dorsal ventral (DV): -1.5 mm), left, and right somatosensory cortices (AP: -0.34 of DBL, ML: ± 0.653 of DBL, DV: -1.5mm). An EMG recording and an EMG reference electrode were inserted into the neck muscles. The mice were allowed to recover from the surgeries for at least one week. Before recording, mice were individually habituated in the recording chambers for 24 hours. EEG/EMG signals (5000-Hz sampling rate with a 0.5-Hz high-pass filter) and videos (30 frames per second) were recorded synchronously for continuous 72 hours using a 4-channel EEG/EMG tethered system (Pinnacle Technology).

Spike-wave discharges (SWDs) were identified by generating putative candidates with custom written code in MATLAB (MathWorks) followed by the classification of candidates with a convolutional neural network in Python that has been trained with manually labeled EEG segments (Chen et al., 2020). Myoclonic seizures were identified by visual inspection of

644 EEG/EMG signals and videos to identify sudden jumps and jerks (Chen et al., 2020). The state
645 of the mouse before each myoclonic seizure event was classified as REM sleep, NREM sleep, or
646 awake based on the EEG/EMG. The video component of the data file for one Vglut2-cHet mouse
647 was corrupted, precluding the identification of myoclonic seizures. Thus, this mouse was only
648 analyzed for SWDs.
649
650 **Statistics**
651 All reported sample numbers (*n*) represent independent biological replicates that are the numbers
652 of tested mice or tissue sections. Statistical analyses were performed with Prism 8 or 9
653 (GraphPad Software) unless stated otherwise below. Anderson-Darling test, D'Agostino-
654 Pearson, Shapiro-Wilk, and Kolmogorov-Smirnov tests were used to determine if data were
655 normally distributed. If all data within one experiment passed all four normality tests, then the
656 statistical test that assumes a Gaussian distribution was used. Otherwise, the statistical test that
657 assumes a non-Gaussian distribution was used. Nested one-way ANOVA with Turkey multiple
658 comparison was used to assess statistical significance of *Stxbp1* expression levels in the DFISH
659 experiments. Either one-way or two-way ANOVA with multiple comparisons was used for
660 Western blot, behavior, and EEG data analyses. For data with Gaussian distribution, ordinary
661 one-way ANOVA with Turkey multiple comparison was used. For non-Gaussian distributed
662 data, Kruskal-Wallis one-way ANOVA with Dunn's multiple comparison test was used. Turkey
663 multiple comparison test was also used in conjunction with two-way ANOVA. For body weight,
664 dystonia score, rotarod test, acoustic startle response, and novel object recognition, two-way
665 repeated measures ANOVA was used with Turkey multiple comparison. Either two-way or
666 three-way ANOVA with Turkey multiple analysis was used for gender effect analyses.

667 OriginPro 2021 (OriginLab) was used to perform three-way ANOVA. To compare the difference
668 between the dystonia scores of Vglut2-cHet and Vgat-cHet mice, Fisher-Freeman-Halton exact
669 test was performed using StatXact 12 (Cytel). The details of all statistical tests, numbers of
670 replicates, and *P* values are reported in **Supplementary File 3**.
671

672 **Acknowledgments**

673 We thank the RNA In Situ Hybridization Core at Baylor College of Medicine for performing the
674 DFISH experiments with the expert assistance of Dr. Cecilia Ljungberg. This work was
675 supported in part by Citizens United for Research in Epilepsy (CURE Epilepsy Award to MX),
676 the National Institute of Neurological Disorders and Stroke (R01NS100893 to MX),
677 the National Institute of Mental Health (R01MH117089 to MX), the Eunice Kennedy Shriver
678 National Institute of Child Health and Human Development (P50HD103555 to Baylor College of
679 Medicine Intellectual and Developmental Disabilities Research Center, Neurovisualization Core
680 and Neurobehavioral Core), and the National Institutes of Health (S10OD016167 to Dr. Cecilia
681 Ljungberg). MX is a Caroline DeLuca Scholar. This article is dedicated to the memory of
682 Caroline DeLuca, who inspired this project.
683
684 **Figures and Legends**

Figure 1

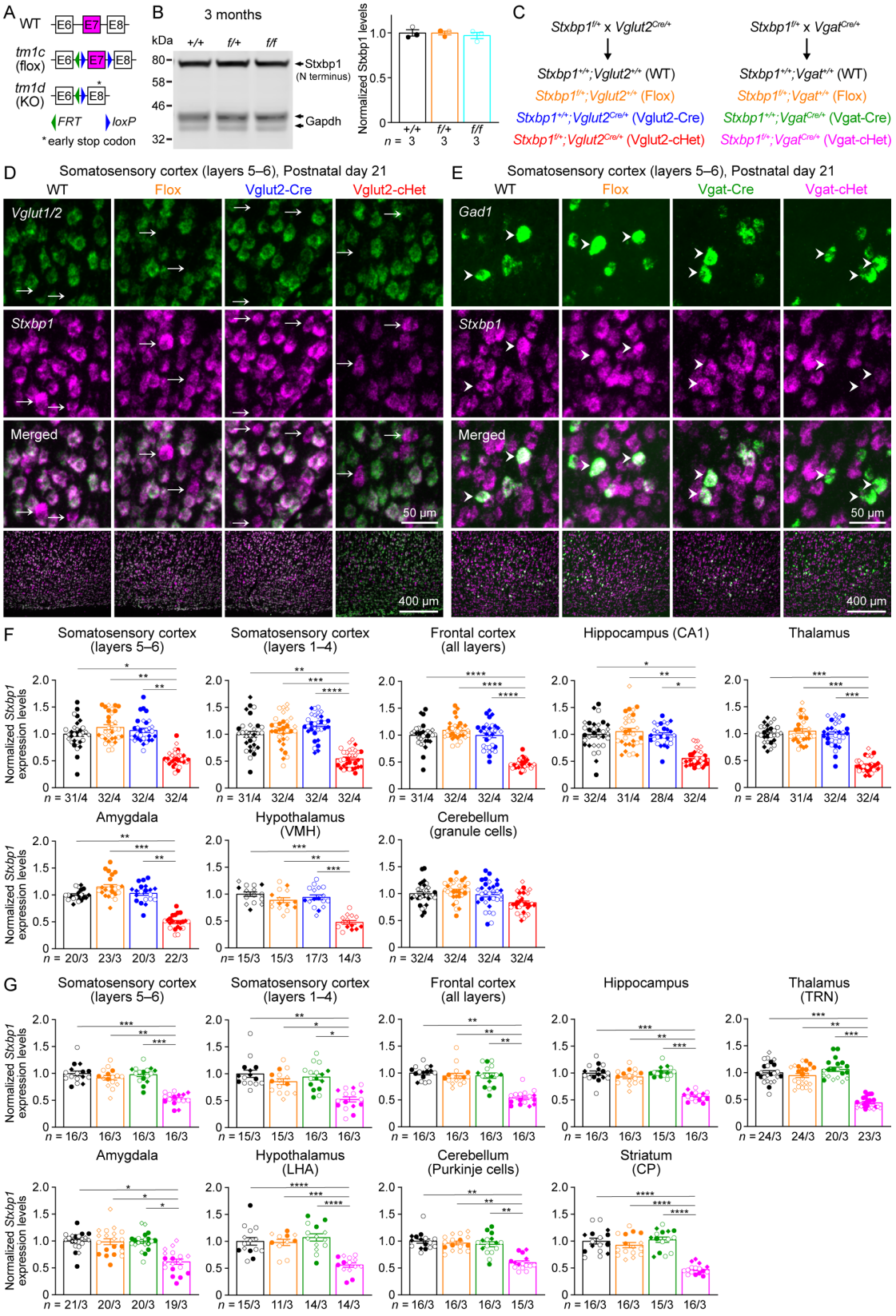

685

Figure 1. Vglut2-cHet and Vgat-cHet mice show specific reduction of *Stxbp1* levels in glutamatergic and GABAergic neurons, respectively, across different brain regions.

(**A**) Genomic structures of *Stxbp1* WT, *tm1c* (flox), and *tm1d* (KO) alleles. In the flox allele, exon 7 is flanked by two *loxP* sites. In the KO allele, exon 7 is deleted, resulting in a premature stop codon in exon 8. E, exon; *FRT*, Flp recombination site; *loxP*, Cre recombination site. (**B**) Left, a representative Western blot of proteins from the cortices of 3-month-old WT, $Stxbp1^{f/+}$, and $Stxbp1^{f/f}$ mice. Stxbp1 was detected by an antibody recognizing its N terminus. Gapdh, a housekeeping protein as loading control. Right, summary data of normalized Stxbp1 protein levels at 3 months of age. Stxbp1 levels were first normalized by the Gapdh levels and then by the average Stxbp1 levels of all WT mice from the same blot. Each filled (male) or open (female) circle represents one mouse. (**C**) $Stxbp1^{f/+}$ mice were crossed to $Vglut2^{Cre/+}$ or $Vgat^{Cre/+}$ mice to generate different genotypes of mice for experiments. The color scheme is maintained across all figures. (**D,E**) Representative fluorescent images from brain sections labeled by ISH probes against *Stxbp1* and *Vglut1/2* (D) or *Gad1* (E). The bottom row shows the layers 5–6 of the somatosensory cortices, and the top three rows show the individual cells from this region. Arrows (D) indicate *Vglut1/2*-negative cells, and arrow heads (E) indicates *Gad1*-positive cells. (**F**) Summary data of normalized *Stxbp1* mRNA levels in *Vglut1/2*-positive cells from different brain regions. *Stxbp1* levels were normalized by the average *Stxbp1* levels of WT brain sections that were simultaneously stained and imaged. The *Stxbp1* levels of Vglut2-cHet mice were reduced in most brain regions except cerebellar granule cells. Different shapes of symbols represent different mice (4 mice per genotype, filled circle and diamond for 2 males and open circle and diamond for 2 females), and each symbol represents one brain section. VMH, ventromedial hypothalamic nucleus. (**G**) Similar to (F), but for *Gad1*-positive cells and 3 mice

709 per genotype. The *Stxbp1* levels of Vgat-cHet mice were reduced in all brain regions. TRN,
710 thalamic reticular nucleus; LHA, lateral hypothalamic area; CP, caudoputamen. Bar graphs are
711 mean ± s.e.m. * $P < 0.05$, ** $P < 0.01$, *** $P < 0.001$, **** $P < 0.0001$.
712

Figure 1-supplement 1

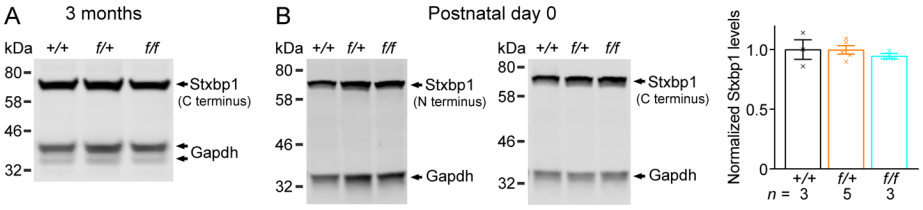

713

714 **Figure 1-supplement 1. Normal Stxbp1 protein levels in *Stxbp1*$^{f/+}$ *and Stxbp1*$^{f/f}$ mice.**
715 (**A**) A representative Western blot of proteins from the cortices of 3-month-old WT, *Stxbp1*$^{f/+}$,
716 and *Stxbp1*$^{f/f}$ mice. Stxbp1 was detected by an antibody recognizing its C terminus. Gapdh, a
717 housekeeping protein as loading control. (**B**) Left, representative Western blots of proteins from
718 the brains of WT, *Stxbp1*$^{f/+}$, and *Stxbp1*$^{f/f}$ mice at postnatal day 0. Stxbp1 was detected by an
719 antibody recognizing its N terminus (left blot) or C terminus (right blot). Right, summary data of
720 normalized Stxbp1 protein levels at postnatal day 0. Stxbp1 levels were first normalized by the
721 Gapdh levels and then by the average Stxbp1 levels of all WT mice from the same blot. Each
722 cross represents one mouse. Bar graphs are mean ± s.e.m.
723

Figure 1-supplement 2

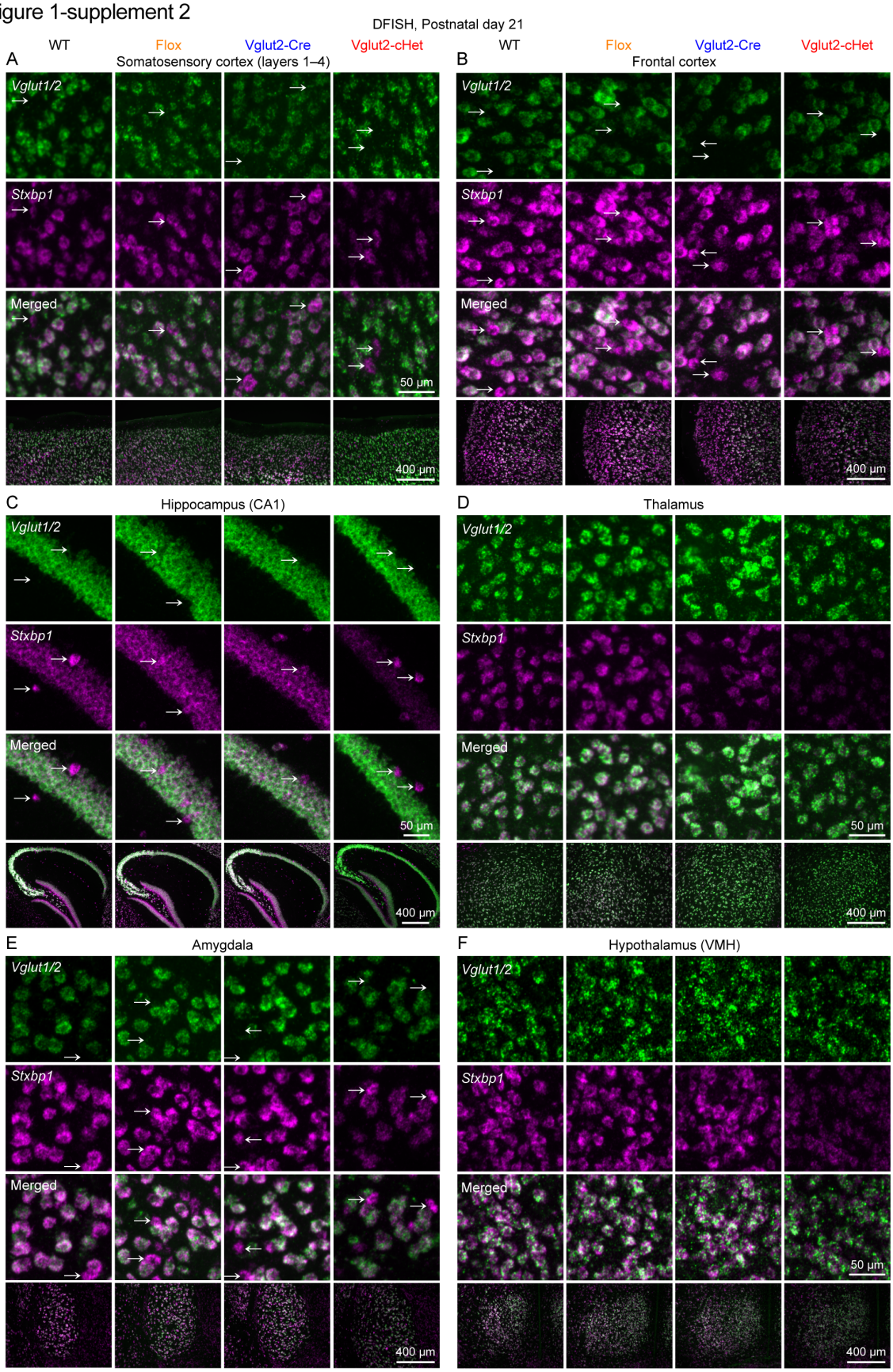

724

Figure 1-supplement 2. Reduction of *Stxbp1* levels specifically in glutamatergic neurons of Vglut2-cHet mice (Part 1).

(**A**) Representative fluorescent images from brain sections labeled by ISH probes against *Stxbp1* and *Vglut1/2*. The bottom row shows the layers 1–4 of the somatosensory cortices, and the top three rows show the individual cells from this region. Arrows indicate *Vglut1/2*-negative cells. (**B–F**) Similar to (A), but for other brain regions indicated on the top of each panel. VMH, ventromedial hypothalamic nucleus.

Figure 1-supplement 3

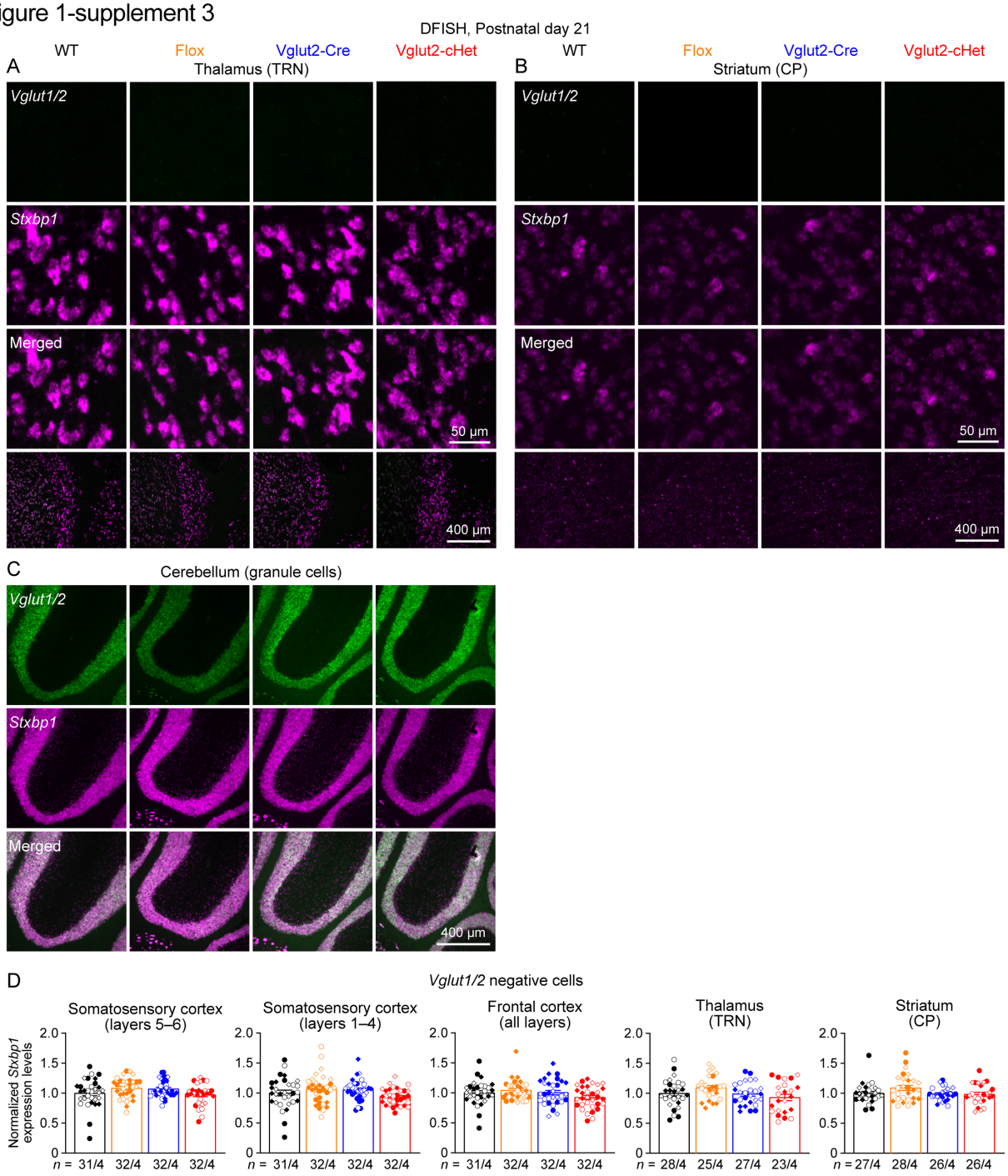

733

734 **Figure 1-supplement 3. Reduction of *Stxbp1* levels specifically in glutamatergic neurons of**

735 **Vglut2-cHet mice (Part 2).**

736 (**A**) Representative fluorescent images from brain sections labeled by ISH probes against *Stxbp1*

737 and *Vglut1/2*. The bottom row shows the thalamic reticular nucleus (TRN), and the top three

738 rows show the individual cells from this region. (**B,C**) Similar to (A), but for other brain regions
739 indicated on the top of each panel. (**D**) Summary data of normalized *Stxbp1* mRNA levels in
740 *Vglut1/2*-negative cells from different brain regions. *Stxbp1* levels were normalized by the
741 average *Stxbp1* levels of WT brain sections that were simultaneously stained and imaged. The
742 *Stxbp1* levels of Vglut2-cHet mice were normal. Different shapes of symbols represent different
743 mice (4 mice per genotype, filled circle and diamond for 2 males and open circle and diamond
744 for 2 females), and each symbol represents one brain section. TRN, thalamic reticular nucleus;
745 CP, caudoputamen. Bar graphs are mean ± s.e.m.
746

Figure 1-supplement 4

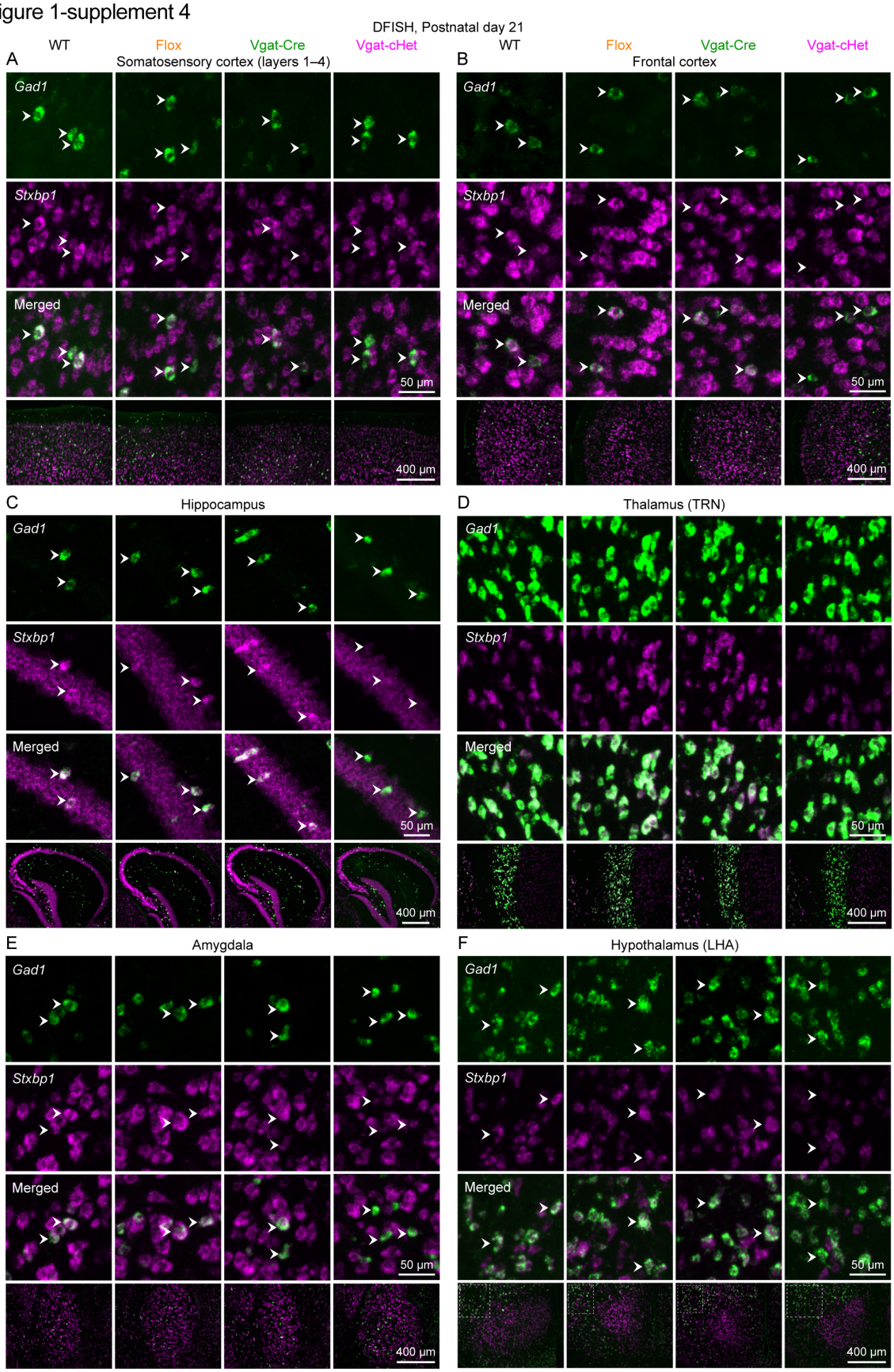

747

748 **Figure 1-supplement 4. Reduction of *Stxbp1* levels specifically in GABAergic neurons of**

749 **Vgat-cHet mice (Part 1).**

750 (**A**) Representative fluorescent images from brain sections labeled by ISH probes against *Stxbp1*

751 and *Gad1*. The bottom row shows the layers 1–4 of the somatosensory cortices, and the top three

752 rows show the individual cells from this region. Arrow heads indicate *Gad1*-positive cells. (**B–**

753 **F**) Similar to (A), but for other brain regions indicated on the top of each panel. TRN, thalamic

754 reticular nucleus; LHA, lateral hypothalamic area.

755

Figure 1-supplement 5

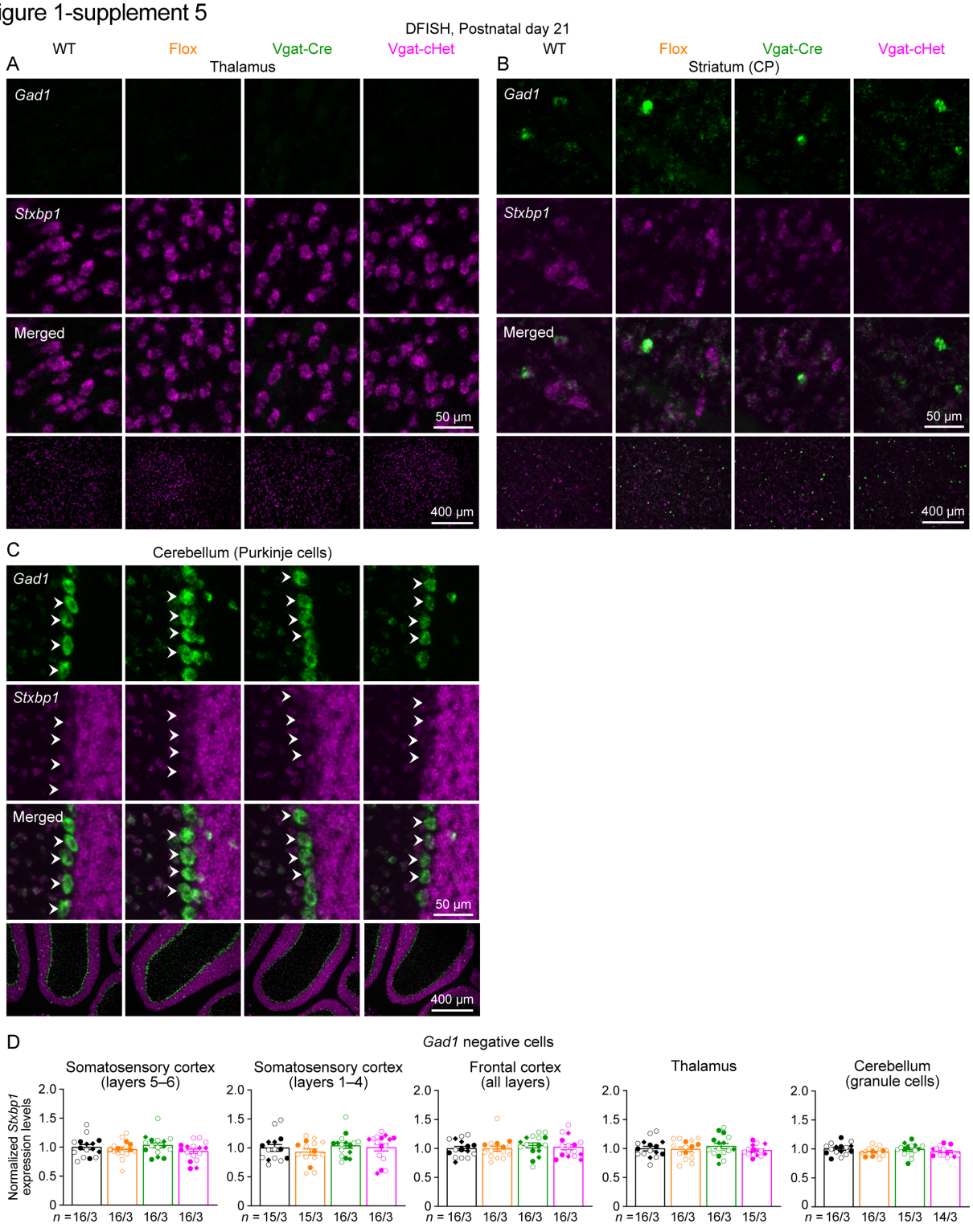

Figure 1-supplement 5. Reduction of *Stxbp1* levels specifically in GABAergic neurons of Vgat-cHet mice (Part 2).

(**A**) Representative fluorescent images from brain sections labeled by ISH probes against *Stxbp1* and *Gad1*. The bottom row shows the thalamus, and the top three rows show the individual cells from this region. (**B,C**) Similar to (A), but for other brain regions indicated on the top of each panel. (**D**) Summary data of normalized *Stxbp1* mRNA levels in *Gad1*-negative cells from different brain regions. *Stxbp1* levels were normalized by the average *Stxbp1* levels of WT brain sections that were simultaneously stained and imaged. The *Stxbp1* levels of Vgat-cHet mice were normal. Different shapes of symbols represent different mice (3 mice per genotype, filled circle and diamond for males and open circle and diamond for females), and each symbol represents one brain section. CP, caudoputamen. Bar graphs are mean ± s.e.m.

Figure 2

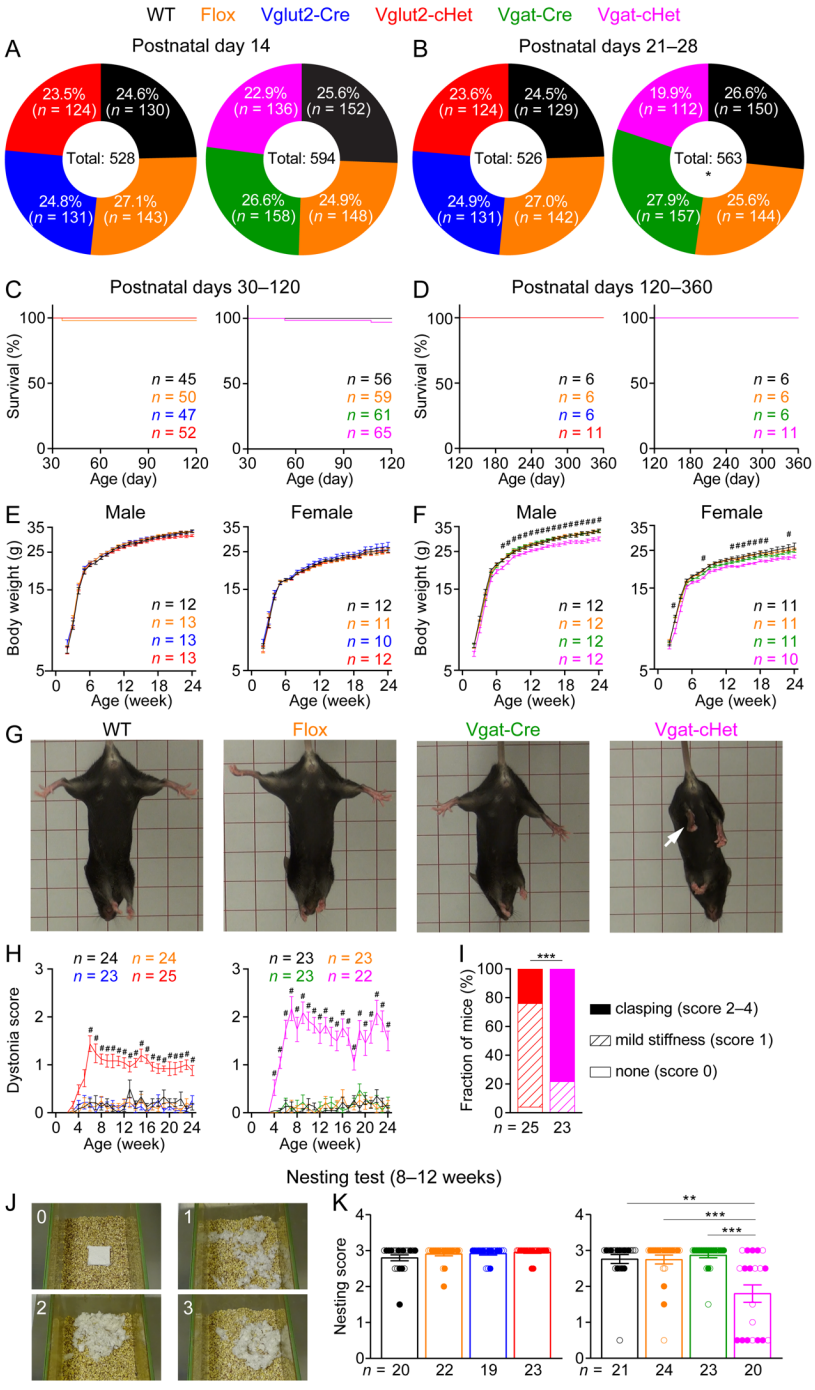

Figure 2. Vgat-cHet mice show reduced survival, reduced body weight, dystonia, and impaired nesting behavior.

(**A,B**) Pie charts show the observed genotypes of different genotypes at postnatal day 14 (A) and

773 postnatal days 21–28 (B). Vgat-cHet mice were significantly less than Mendelian expectations at
774 postnatal days 21–28. (**C,D**) Both Vglut2-cHet (C) and Vgat-cHet (D) mice had normal survival
775 rates after postnatal day 30. (**E,F**) Body weight as a function of age. The body weight of Vgat-
776 cHet mice was less than that of control mice (F). # indicates that Vgat-cHet mice are statistically
777 different (i.e., at least $P < 0.05$) from at least both Flox and Vgat-Cre mice. (**G**) Vgat-cHet
778 showed dystonia and hindlimb clasping (arrows). (**H**) Dystonia scores as a function of age. #
779 indicates that Vglut2-cHet and Vgat-cHet mice are statistically different (i.e., at least $P < 0.05$)
780 from at least both corresponding Flox and Cre mice. (**I**) The fractions of Vglut2-cHet and Vgat-
781 cHet mice with different severities of dystonia. (**J,K**) The quality of the nests was scored
782 according to the criteria in (J). Vgat-cHet mice built poor quality nests within 24 hours. The
783 numbers and ages of tested mice are indicated in the figures. Each filled (male) or open (female)
784 circle represents one mouse. Bar graphs are mean ± s.e.m. * $P < 0.05$, ** $P < 0.01$, *** $P <$
785 0.001, **** $P < 0.0001$.
786

Figure 3

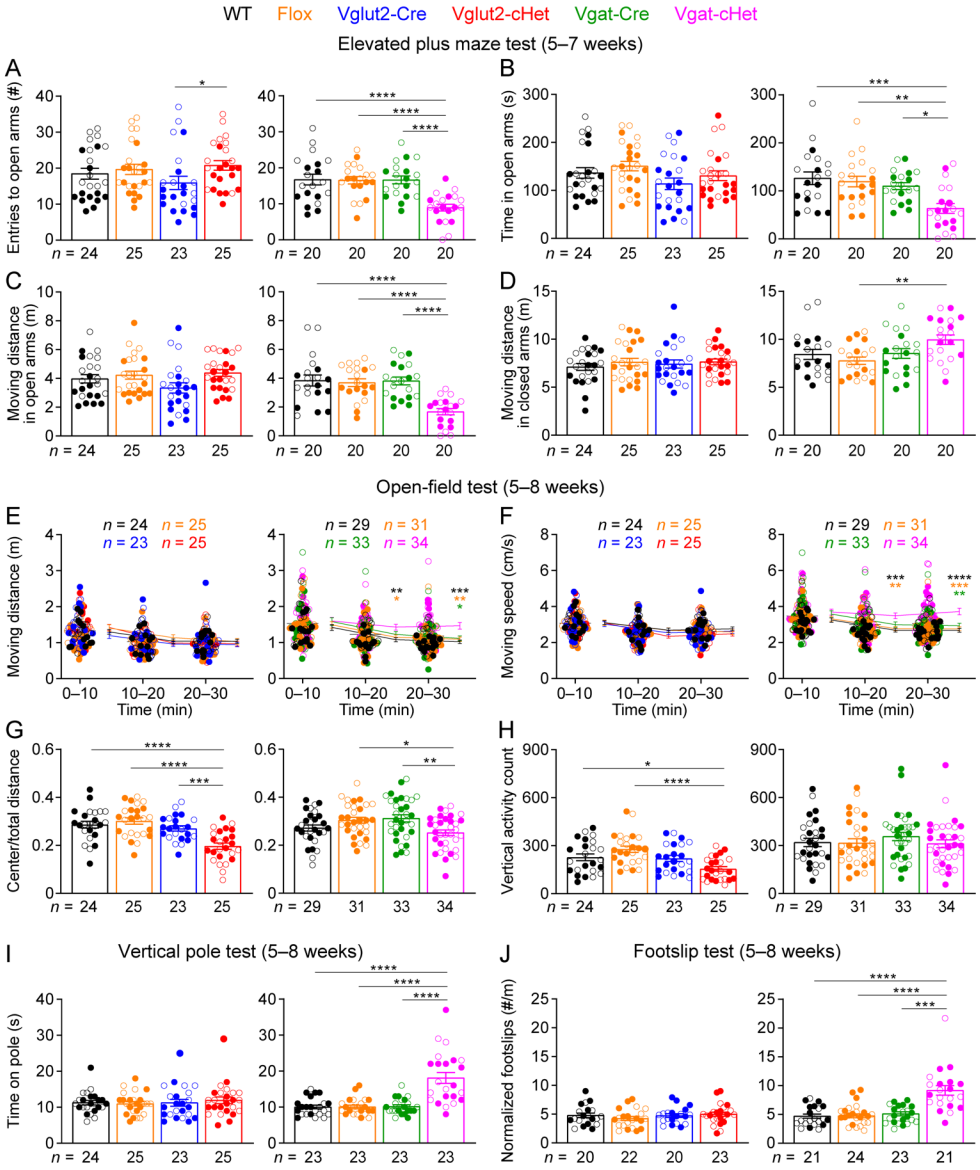

Figure 3. Vgat-cHet mice show elevated anxiety-like behaviors, hyperactivity, and motor dysfunctions.

(**A**–**D**) In the elevated plus maze test, Vgat-cHet mice, but not Vglut2-cHet mice, entered the open arms less frequently (A), spent less time (B), and traveled shorter distance (C) in the open arms than control mice. In the closed arms, the travel distances of Vglut2-cHet mice were similar to those of control mice, and Vgat-cHet mice traveled slightly longer distances than Flox mice

(D). (**E**,**F**) In the open-field test, Vgat-cHet mice, but not Vglut2-cHet mice, showed an increase in the moving distance (E) and speed (F). The statistical significance between Vgat-cHet and WT, Flox, or Vgat-Cre mice is indicated by black, orange, or green asterisks, respectively. (**G**) Vglut2-cHet and Vgat-cHet mice showed a decrease in the ratio of center moving distances over total moving distance. (**H**) Vglut2-cHet mice, but not Vgat-cHet mice, showed a decrease in the vertical activity. (**I,J**) Vgat-cHet mice, but not Vglut2-cHet mice, took more time to come down from a vertical pole (I) and made more foot slips per travel distance on a wire grid (J). The numbers and ages of tested mice are indicated in the figures. Each filled (male) or open (female) circle represents one mouse. Bar graphs are mean ± s.e.m. * $P < 0.05$, ** $P < 0.01$, *** $P < 0.001$, **** $P < 0.0001$.

Figure 3-supplement 1

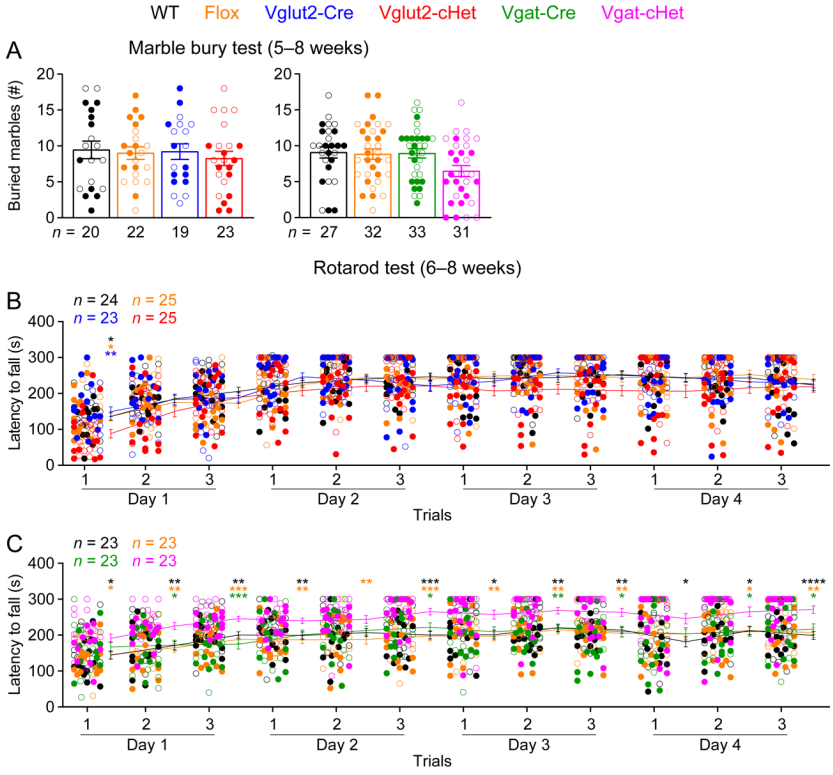

Figure 3-supplement 1. Vglut2-cHet and Vgat-cHet mice do not show impairments in marble bury and rotarod tests.

(**A**) The numbers of buried marbles by Vglut2-cHet and Vgat-cHet mice were not significantly different from those of control mice. (**B,C**) In the rotarod test, Vglut2-cHet mice performed similar to control mice except the first trial (B) and Vgat-cHet mice performed better than control mice, as they were able to stay on the rotating rod for longer time (C), probably due to their lower body weight or hyperactivity. The statistical significance between Vglut2-cHet and WT, Flox, or Vglut2-Cre mice is indicated by black, orange, or blue asterisks, respectively, and between Vgat-cHet and WT, Flox, or Vgat-Cre mice by black, orange, or green asterisks, respectively. The numbers and ages of tested mice are indicated in the figures. Each filled (male) or open (female) circle represents one mouse. Bar graphs are mean ± s.e.m. * $P < 0.05$, ** $P < 0.01$, *** $P < 0.001$, **** $P < 0.0001$.

Figure 3-supplement 2

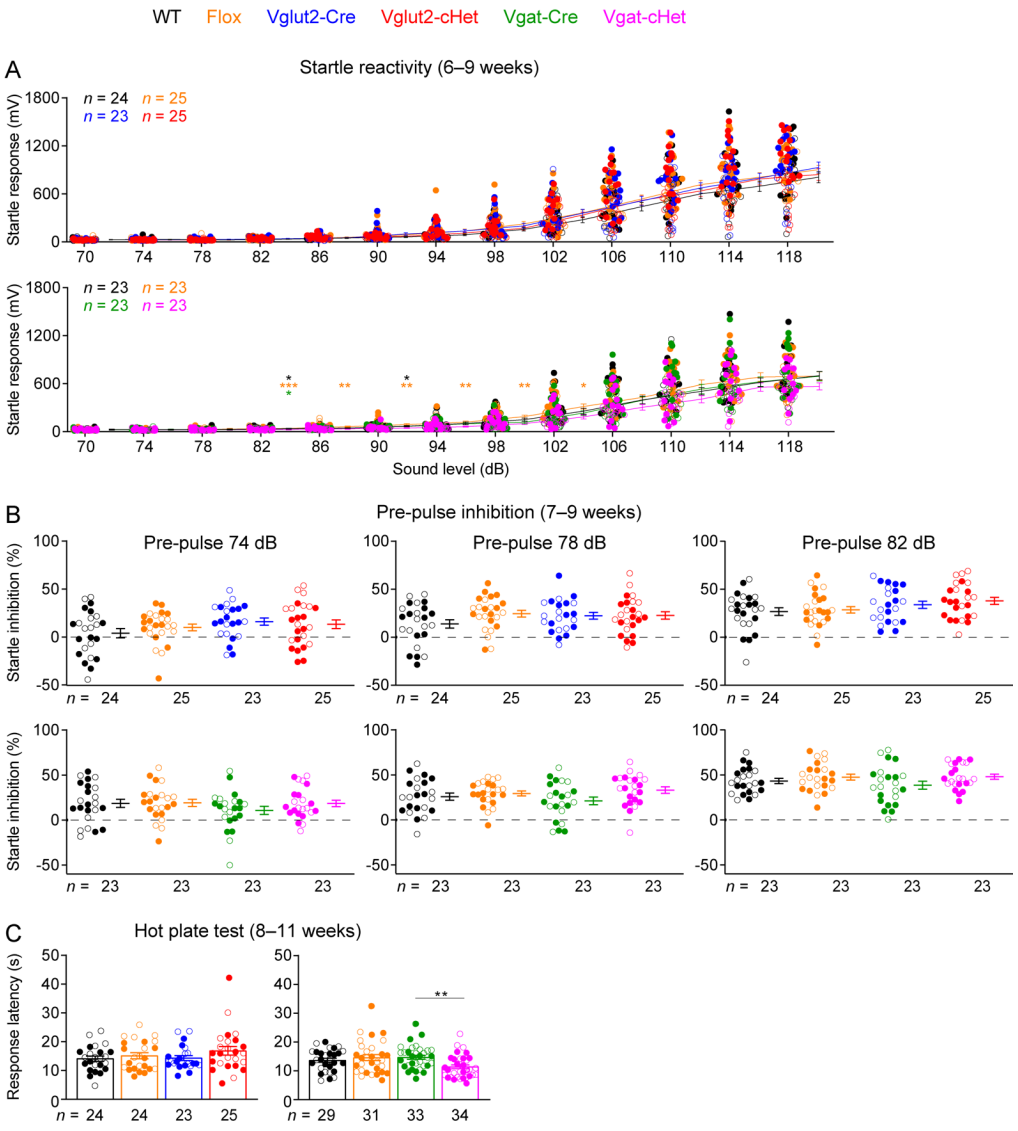

819

820 **Figure 3-supplement 2. Vglut2-cHet and Vgat-cHet mice have normal sensory functions.**

821 (**A**) Vglut2-cHet and Vgat-cHet mice showed similar acoustic startle responses as control mice at

822 different sound levels. The statistical significance between Vgat-cHet and WT, Flox, or Vgat-Cre

823 mice is indicated by black, orange, or green asterisks, respectively. (**B**) In the pre-pulse inhibition

824 test, when a weak sound (i.e., pre-pulse 74, 78, or 82 dB) preceded a loud sound (120 dB),

825 Vglut2-cHet and Vgat-cHet mice showed a similar reduction in the startle responses to the loud

826 sound as control mice. (**C**) In the hot plate test, Vglut2-cHet mice showed similar latencies in
827 response to the high temperature as control mice, and the latencies of Vgat-cHet were slightly
828 shorter than Vgat-Cre mice. The numbers and ages of tested mice are indicated in the figures.
829 Each filled (male) or open (female) circle represents one mouse. Bar graphs are mean ± s.e.m. *
830 $P < 0.05$, ** $P < 0.01$, *** $P < 0.001$.
831

Figure 4

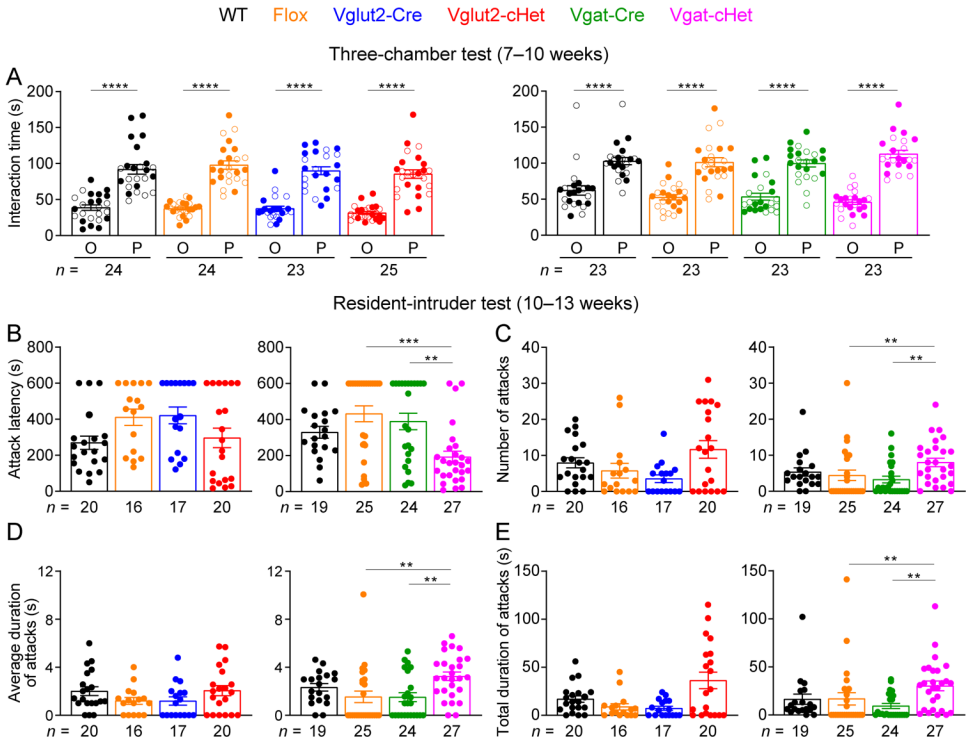

832

833 **Figure 4. Vgat-cHet mice show normal sociability but increased aggressive behaviors.**
834 (**A**) In the three-chamber test, Vglut2-cHet, Vgat-cHet, and control mice showed a preference in
835 interacting with the partner mouse over the object. (**B**–**E**) In the resident-intruder test, male Vgat-
836 cHet mice, but not Vglut2-cHet mice, showed a reduction in the latency to attack the male
837 intruder mice (B). The number (C), average duration (D), and total duration (E) of attacks were
838 increased as compared to control mice. The numbers and ages of tested mice are indicated in the

839 figures. Each filled (male) or open (female) circle represents one mouse. Bar graphs are mean ±

840 s.e.m. ** $P < 0.01$, *** $P < 0.001$, **** $P < 0.0001$.

841

Figure 5

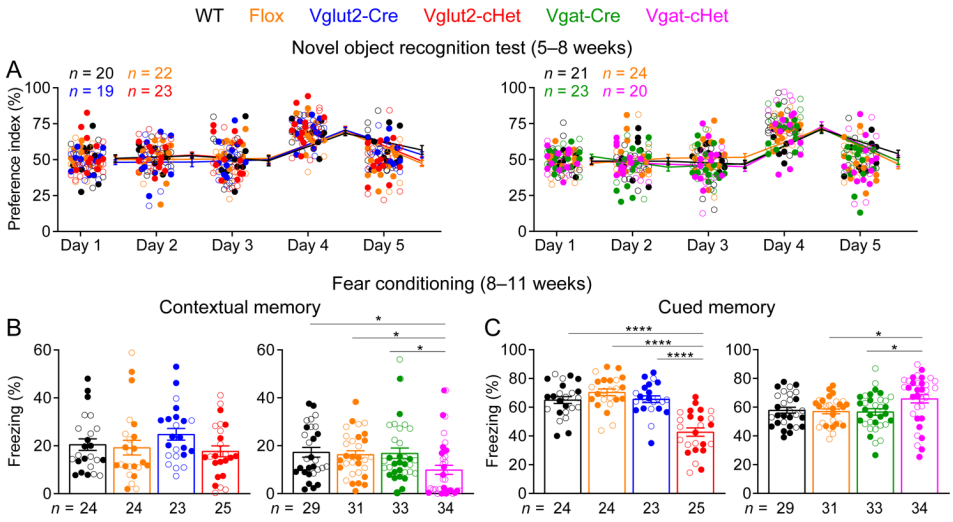

842

843 **Figure 5. Distinct cognitive deficits of Vglut2-cHet and Vgat-cHet mice.**

844 (**A**) In the novel object recognition test with 24-hour testing intervals, the ability of a mouse to

845 recognize the novel object was measured by the preference index (see Materials and methods).

846 Mice were presented with the same two identical objects on days 1, 2, 3, and 5, and the familiar

847 object and a novel object on day 4. Similar to control mice, Vglut2-cHet and Vgat-cHet mice

848 showed a preference for the novel object. (**B,C**) In the fear conditioning test, Vgat-cHet and

849 Vglut2-cHet mice showed a reduction in context-induced (B) and cue-induced (C) freezing

850 behaviors 24 hours after training, respectively. Vgat-cHet also showed a modest increase in cue-

851 induced freezing. The numbers and ages of tested mice are indicated in the figures. Each filled

852 (male) or open (female) circle represents one mouse. Bar graphs are mean ± s.e.m. * $P < 0.05$,

853 **** $P < 0.0001$.

854

Figure 5-supplement 1

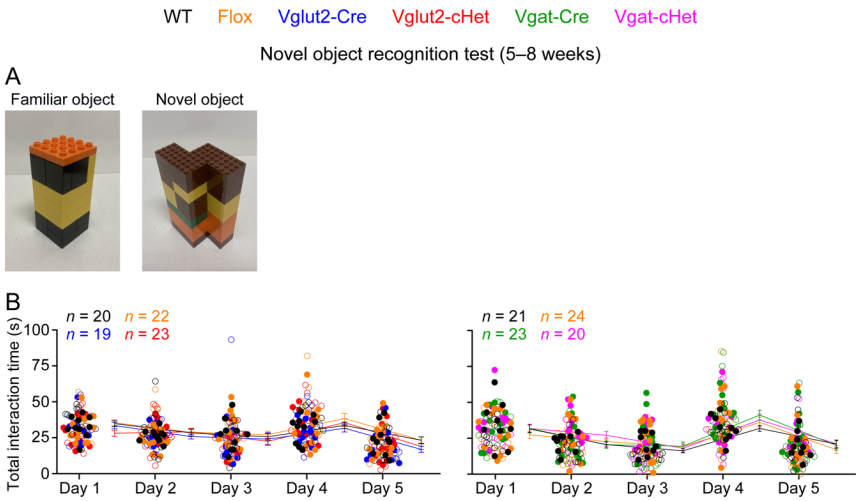

Figure 5-supplement 1. Normal novel objection recognition in Vglut2-cHet and Vgat-cHet mice.

(**A**) The images of the familiar and novel objects used in the novel objection recognition test. (**B**) The total interaction time with familiar and novel objects of Vglut2-cHet or Vgat-cHet mice was similar to that of control mice. The numbers and ages of tested mice are indicated in the figures. Each filled (male) or open (female) circle represents one mouse. Bar graphs are mean ± s.e.m.

Figure 6

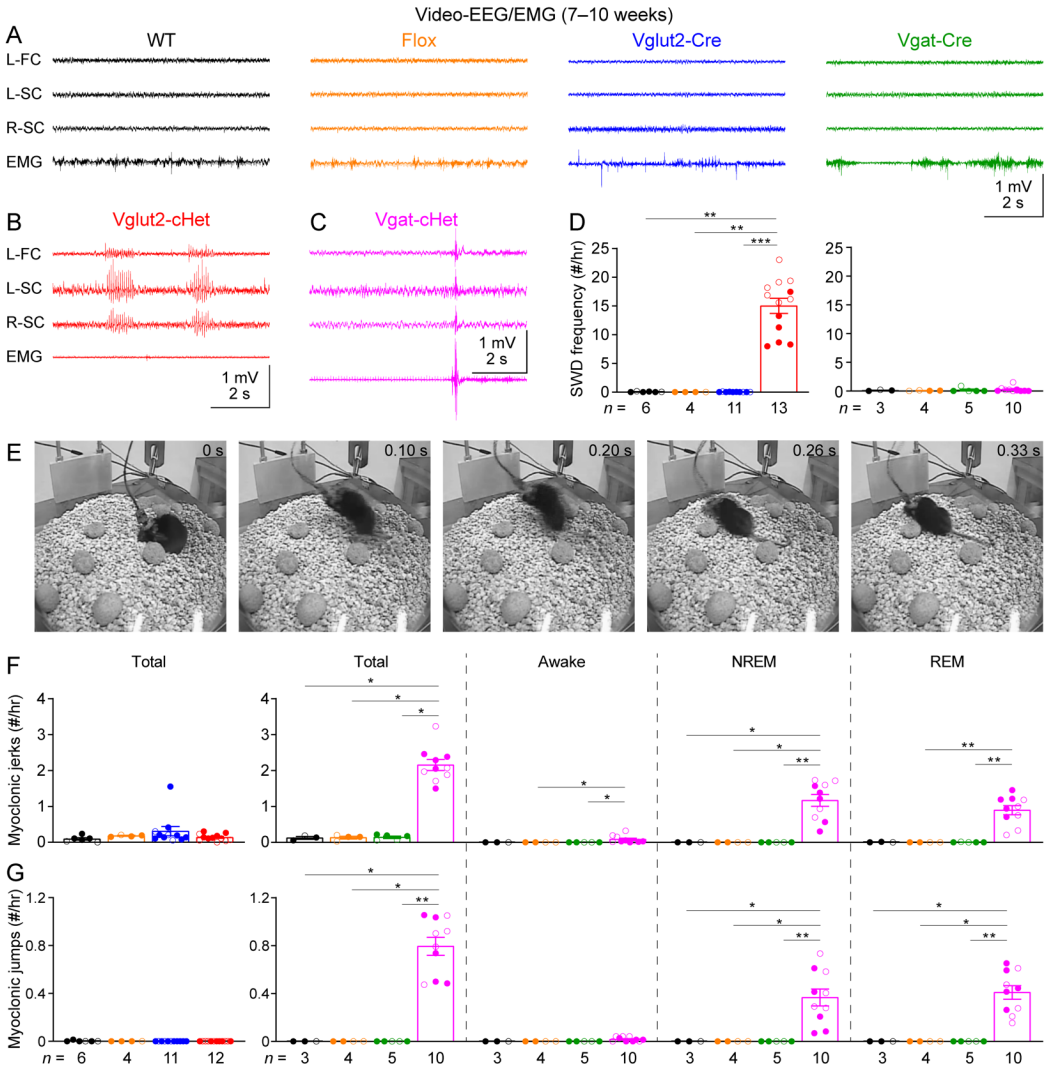

Figure 6. Vglut2-cHet and Vgat-cHet mice exhibit different forms of epileptic seizures.

(**A**) Representative EEG traces from the left frontal cortex (L-FC), left somatosensory cortex (L-SC), right somatosensory cortex (R-SC), and EMG traces from the neck muscle of control mice. (**B,C**) Representative EEG and EMG traces showing two spike-wave discharges (SWDs, indicated by the blue arrows) of a Vglut2-cHet mouse (B) and a myoclonic jerk (indicated by the blue arrow) of a Vgat-cHet mouse (C). The Vgat-cHet mouse was in REM sleep before the jerk. (**D**) Summary data showing that the SWD frequencies of Vglut2-cHet mice were drastically

871 increased as compared to control mice. (**E**) Video frames showing a myoclonic jump of a Vgat-
872 cHet mouse (see ***Video 3***). The mouse was in REM sleep before the jump. (**F,G**) Summary data
873 showing the total frequencies of myoclonic jerks (F) and jumps (G) and the frequencies in
874 different behavioral states. The frequencies of both jerks and jumps were drastically increased in
875 Vgat-cHet mice, particularly during NREM and REM sleep. The numbers and ages of recorded
876 mice are indicated in the figures. Each filled (male) or open (female) circle represents one
877 mouse. Bar graphs are mean ± s.e.m. * $P < 0.05$, ** $P < 0.01$, *** $P < 0.001$.
878

Figure 7

879 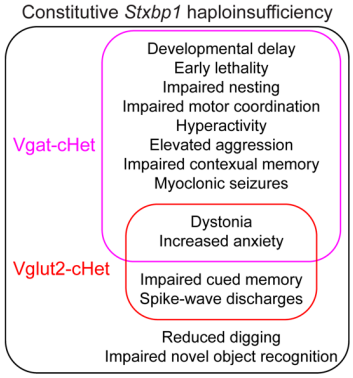

880 **Figure 7. Comparison of constitutive *Stxbp1* haploinsufficient mice, Vglut2-cHet mice, and**
881 **Vgat-cHet mice.**

882 Square Venn diagram showing the phenotypes of constitutive *Stxbp1* haploinsufficient mice,
883 Vglut2-cHet mice, and Vgat-cHet mice. Except the reduced digging behavior and impaired novel
884 object recognition, Vglut2-cHet and Vgat-cHet mice together recapitulate all other phenotypes of
885 constitutive haploinsufficient mice. Vglut2-cHet and Vgat-cHet mice each recapitulate distinct
886 subsets of the phenotypes of constitutive haploinsufficient mice. Only dystonia and increased
887 anxiety are shared between Vglut2-cHet and Vgat-cHet mice. Vgat-cHet mice exhibit broader
888 and more severe phenotypes than Vglut2-cHet mice.

889

890 **Supplementary File 1. Double fluorescent *in situ* hybridization probe sequences**

891 The sequences of the *Stxbp1*, *Vglut1*, *Vglut2*, and *Gad1* probes are provided.

892

893 **Supplementary File 2. Phenotypic comparison of human patients and different mouse**

894 **models.**

895 The phenotyping tests in different mouse models (the second column) are grouped based on the

896 clinical features of *STXBP1* encephalopathy (the first column). The results of the phenotyping

897 tests from different mouse models are compared in the table.

898

899 **Supplementary File 3. Statistics of experimental results.**

900 The details of all statistical tests, numbers of replicates, and *P* values are presented for each

901 experiment in the table.

902

903 **Video 1. Vglut2-cHet mice show SWDs.**

904 A representative video showing several SWDs in a Vglut2-cHet mouse. The top 3 traces are

905 EEG signals from the left frontal cortex, right somatosensory cortex, and left somatosensory

906 cortex. The bottom trace is the EMG signal from the neck muscle. The vertical line indicates the

907 time of the current video frame. Note that the EEG signal from the left somatosensory cortex (the

908 third channel) is inverted.

909

910 **Video 2. Vgat-cHet mice show myoclonic jerks.**

911 A representative video showing a myoclonic jerk of a Vgat-cHet mouse. The top 3 traces are

912 EEG signals from the left frontal cortex, right somatosensory cortex, and left somatosensory
913 cortex. The bottom trace is the EMG signal from the neck muscle. The vertical line indicates the
914 time of the current video frame. The mouse was in REM sleep before the jerk. Note that the EEG
915 signal from the left somatosensory cortex (the third channel) is inverted.
916
917 **Video 3. Vgat-cHet mice show myoclonic jumps.**
918 A representative video showing a myoclonic jump of a Vgat-cHet mouse. The top 3 traces are
919 EEG signals from the left frontal cortex, right somatosensory cortex, and left somatosensory
920 cortex. The bottom trace is the EMG signal from the neck muscle. The vertical line indicates the
921 time of the current video frame. The mouse was in REM sleep before the jump. Note that the
922 EEG signal from the left somatosensory cortex (the third channel) is inverted.

References

Abramov D, Guiberson NGL, Burré J (2020) STXBP1 encephalopathies: Clinical spectrum, disease mechanisms, and therapeutic strategies. Journal of Neurochemistry.

Antunes M, Biala G (2012) The novel object recognition memory: neurobiology, test procedure, and its modifications. Cogn Process 13:93–110.

Bonnycastle K, Davenport EC, Cousin MA (2021) Presynaptic dysfunction in neurodevelopmental disorders: Insights from the synaptic vesicle life cycle. Journal of Neurochemistry 157:179–207.

Boulland J-L, Qureshi T, Seal RP, Rafiki A, Gundersen V, Bergersen LH, Fremeau RT, Edwards RH, Storm-Mathisen J, Chaudhry FA (2004) Expression of the vesicular glutamate transporters during development indicates the widespread corelease of multiple neurotransmitters. J Comp Neurol 480:264–280.

Brose N, O'Connor V, Skehel P (2010) Synaptopathy: dysfunction of synaptic function? Biochem Soc Trans 38:443–444.

Chai YJ, Sierecki E, Tomatis VM, Gormal RS, Giles N, Morrow IC, Xia D, Götz J, Parton RG, Collins BM, Gambin Y, Meunier FA (2016) Munc18-1 is a molecular chaperone for α-synuclein, controlling its self-replicating aggregation. J Cell Biol 214:705–718.

Chao H-T, Chen H, Samaco RC, Xue M, Chahrour M, Yoo J, Neul JL, Gong S, Lu H-C, Heintz N, Ekker M, Rubenstein JLR, Noebels JL, Rosenmund C, Zoghbi HY (2010) Dysfunction in GABA signalling mediates autism-like stereotypies and Rett syndrome phenotypes. Nature 468:263–269.

Chen W, Cai Z-L, Chao ES, Chen H, Longley CM, Hao S, Chao H-T, Kim JH, Messier JE, Zoghbi HY, Tang J, Swann JW, Xue M (2020) Stxbp1/Munc18-1 haploinsufficiency impairs inhibition and mediates key neurological features of STXBP1 encephalopathy. Elife 9.

Cohen SJ, Stackman RW (2015) Assessing rodent hippocampal involvement in the novel object recognition task. A review. Behav Brain Res 285:105–117.

Deciphering Developmental Disorders Study (2015) Large-scale discovery of novel genetic causes of developmental disorders. Nature 519:223–228.

Gemelli T, Berton O, Nelson ED, Perrotti LI, Jaenisch R, Monteggia LM (2006) Postnatal loss of methyl-CpG binding protein 2 in the forebrain is sufficient to mediate behavioral aspects of Rett syndrome in mice. Biol Psychiatry 59:468–476.

Grant SGN (2019) Synapse diversity and synaptome architecture in human genetic disorders. Hum Mol Genet 28:R219–R225.

Grone BP, Marchese M, Hamling KR, Kumar MG, Krasniak CS, Sicca F, Santorelli FM, Patel M, Baraban SC (2016) Epilepsy, Behavioral Abnormalities, and Physiological Comorbidities in Syntaxin-Binding Protein 1 (STXBP1) Mutant Zebrafish. PLoS ONE 11:e0151148.

Guiberson NGL, Pineda A, Abramov D, Kharel P, Carnazza KE, Wragg RT, Dittman JS, Burré J (2018) Mechanism-based rescue of Munc18-1 dysfunction in varied encephalopathies by chemical chaperones. Nature Communications 9:3986.

Hager T, Maroteaux G, Pont PD, Julsing J, van Vliet R, Stiedl O (2014) Munc18-1 haploinsufficiency results in enhanced anxiety-like behavior as determined by heart rate responses in mice. Behav Brain Res 260:44–52.

Harrison SD, Broadie K, van de Goor J, Rubin GM (1994) Mutations in the Drosophila Rop gene suggest a function in general secretion and synaptic transmission. Neuron 13:555–566.

John A, Ng-Cordell E, Hanna N, Brkic D, Baker K (2021) The neurodevelopmental spectrum of synaptic vesicle cycling disorders. Journal of Neurochemistry 157:208–228.

Kaplanis J et al. (2020) Evidence for 28 genetic disorders discovered by combining healthcare and research data. Nature 586:757–762.

Kovačević J, Maroteaux G, Schut D, Loos M, Dubey M, Pitsch J, Remmelink E, Koopmans B, Crowley J, Cornelisse LN, Sullivan PF, Schoch S, Toonen RF, Stiedl O, Verhage M (2018) Protein instability, haploinsufficiency, and cortical hyper-excitability underlie STXBP1 encephalopathy. Brain 141:1350–1374.

Lepeta K et al. (2016) Synaptopathies: synaptic dysfunction in neurological disorders - A review from students to students. Journal of Neurochemistry 138:785–805.

Marchese M, Valvo G, Moro F, Sicca F, Santorelli FM (2016) Targeted Gene Resequencing (Astrochip) to Explore the Tripartite Synapse in Autism-Epilepsy Phenotype with Macrocephaly. Neuromolecular Med 18:69–80.

Melland H, Carr EM, Gordon SL (2021) Disorders of synaptic vesicle fusion machinery. Journal of Neurochemistry 157:130–164.

Meng X, Wang W, Lu H, He L-J, Chen W, Chao E, Fiorotto ML, Tang B, Herrera JA, Seymour ML, Neul JL, Pereira FA, Tang J, Xue M, Zoghbi HY (2016) Manipulations of MeCP2 in glutamatergic neurons highlight their contributions to Rett and other neurological disorders. Elife 5:185.

Miyamoto H, Shimohata A, Abe M, Abe T, Mazaki E, Amano K, Suzuki T, Tatsukawa T, Itohara S, Sakimura K, Yamakawa K (2017) Potentiation of excitatory synaptic transmission ameliorates aggression in mice with Stxbp1 haploinsufficiency. Hum Mol Genet 26:4961–4974.

Miyamoto H, Tatsukawa T, Shimohata A, Yamagata T, Suzuki T, Amano K, Mazaki E, Raveau M, Ogiwara I, Oba-Asaka A, Hensch TK, Itohara S, Sakimura K, Kobayashi K, Kobayashi

992 K, Yamakawa K (2019) Impaired cortico-striatal excitatory transmission triggers epilepsy.
993 Nature Communications 10:1917.

994 Orock A, Logan S, Deák F (2018) Munc18-1 haploinsufficiency impairs learning and memory
995 by reduced synaptic vesicular release in a model of Ohtahara syndrome. Mol Cell Neurosci
996 88:33–42.

997 Patzke C, Han Y, Covy J, Yi F, Maxeiner S, Wernig M, Südhof TC (2015) Analysis of
998 conditional heterozygous STXBP1 mutations in human neurons. J Clin Invest 125:3560–
999 3571.

1000 Ramos-Miguel A, Hercher C, Beasley CL, Barr AM, Bayer TA, Falkai P, Leurgans SE,
1001 Schneider JA, Bennett DA, Honer WG (2015) Loss of Munc18-1 long splice variant in
1002 GABAergic terminals is associated with cognitive decline and increased risk of dementia in
1003 a community sample. Mol Neurodegener 10:65.

1004 Raymond CS, Soriano P (2007) High-efficiency FLP and PhiC31 site-specific recombination in
1005 mammalian cells. PLoS ONE 2:e162.

1006 Stamberger H et al. (2016) STXBP1 encephalopathy: A neurodevelopmental disorder including
1007 epilepsy. Neurology 86:954–962.

1008 Suri M, Evers JMG, Laskowski RA, O'Brien S, Baker K, Clayton-Smith J, Dabir T, Josifova D,
1009 Joss S, Kerr B, Kraus A, McEntagart M, Morton J, Smith A, Splitt M, Thornton JM, DDD
1010 Study, Wright CF (2017) Protein structure and phenotypic analysis of pathogenic and
1011 population missense variants in STXBP1. Mol Genet Genomic Med 5:495–507.

1012 Symonds JD, McTague A (2020) Epilepsy and developmental disorders: Next generation
1013 sequencing in the clinic. Eur J Paediatr Neurol 24:15–23.

1014 Toonen RFG, Wierda K, Sons MS, de Wit H, Cornelisse LN, Brussaard A, Plomp JJ, Verhage M
1015 (2006) Munc18-1 expression levels control synapse recovery by regulating readily releasable
1016 pool size. Proc Natl Acad Sci USA 103:18332–18337.

1017 Verhage M, Maia AS, Plomp JJ, Brussaard AB, Heeroma JH, Vermeer H, Toonen RF, Hammer
1018 RE, van den Berg TK, Missler M, Geuze HJ, Sudhof TC (2000) Synaptic assembly of the
1019 brain in the absence of neurotransmitter secretion. Science 287:864–869.

1020 Verhage M, Sørensen JB (2020) SNAREopathies: Diversity in Mechanisms and Symptoms.
1021 Neuron:1–16.

1022 Vong L, Ye C, Yang Z, Choi B, Chua S, Lowell BB (2011) Leptin action on GABAergic
1023 neurons prevents obesity and reduces inhibitory tone to POMC neurons. Neuron 71:142–
1024 154.

1025 Weimer RM, Richmond JE, Davis WS, Hadwiger G, Nonet ML, Jorgensen EM (2003) Defects
1026 in synaptic vesicle docking in unc-18 mutants. Nat Neurosci 6:1023–1030.

1027 Yaylaoglu MB, Titmus A, Visel A, Alvarez-Bolado G, Thaller C, Eichele G (2005)
1028 Comprehensive expression atlas of fibroblast growth factors and their receptors generated by
1029 a novel robotic in situ hybridization platform. Dev Dyn 234:371–386.

1030 Zhu B, Mak JCH, Morris AP, Marson AG, Barclay JW, Sills GJ, Morgan A (2020) Functional
1031 analysis of epilepsy-associated variants in STXBP1/Munc18-1 using humanized
1032 Caenorhabditis elegans. Epilepsia.

1033